Pyramidal neurons proportionately alter the identity and survival of specific cortical interneuron subtypes

Sherry Jingjing Wu[1,2,*], Min Dai[1,2,*], Shang-Po Yang[2], Cai McCann[3], Yanjie Qiu[1,2], Giovanni J. Marrero[4], Jeffrey A. Stogsdill[2,6], Daniela J. Di Bella[2,6], Qing Xu[5], Samouil L. Farhi[3], Evan Z. Macosko[2], Fei Chen[4,6], and Gord Fishell[1,2]

[1]Harvard Medical School, Blavatnik Institute, Department of Neurobiology, Boston, MA 02115, USA.
[2]Stanley Center for Psychiatric Research, Broad Institute of MIT and Harvard, Cambridge, MA 02142, USA.
[3]Spatial Technology Platform, Broad Institute of MIT and Harvard, Cambridge, MA 02142, USA.
[4]Broad Institute of MIT and Harvard, Cambridge, MA 02142, USA
[5]Center for Genomics & Systems Biology, New York University Abu Dhabi, Abu Dhabi, UAE
[6]Department of Stem Cell and Regenerative Biology, Harvard University, Cambridge, MA 02138, USA
*These authors contributed equally to this work

Corresponding Author
Gord Fishell, Ph.D.
Professor of Neurobiology and Broad Institute Member
Harvard Medical School and the Stanley Center at the Broad
Rm 201, Armenise Bldg., 220 Longwood Ave, Boston, MA 02115, USA
Phone: 617 432-5335 (HMS)
Phone: 617 714-7052 (Broad)
Email: gordon_fishell@hms.harvard.edu

25 **Abstract**

26 The mammalian cerebral cortex comprises a complex neuronal network that maintains a delicate balance between excitatory

27 neurons and inhibitory interneurons. Previous studies, including our own research, have shown that specific interneuron

28 subtypes are closely associated with particular pyramidal neuron types, forming stereotyped local inhibitory microcircuits.

29 However, the developmental processes that establish these precise networks are not well understood. Here we show that

30 pyramidal neuron types are instrumental in driving the terminal differentiation and maintaining the survival of specific

31 associated interneuron subtypes. In a wild-type cortex, the relative abundance of different interneuron subtypes aligns

32 precisely with the pyramidal neuron types to which they synaptically target. In *Fezf2* mutant cortex, characterized by the

33 absence of layer 5 pyramidal tract neurons and an expansion of layer 6 intratelencephalic neurons, we observed a

34 corresponding decrease in associated layer 5b interneurons and an increase in layer 6 subtypes. Interestingly, these shifts in

35 composition are achieved through mechanisms specific to different interneuron types. While SST interneurons adjust their

36 abundance to the change in pyramidal neuron prevalence through the regulation of programmed cell death, parvalbumin

37 interneurons alter their identity. These findings illustrate two key strategies by which the dynamic interplay between

38 pyramidal neurons and interneurons allows local microcircuits to be sculpted precisely. These insights underscore the

39 precise roles of extrinsic signals from pyramidal cells in the establishment of interneuron diversity and their subsequent

40 integration into local cortical microcircuits.

41

42

43 Single-cell sequencing studies have elucidated the transcriptomic landscape of cortical neurons across the isocortex,

44 revealing considerable diversity among both excitatory neurons and inhibitory interneurons[1–3]. These studies also showed

45 that while excitatory neuron subtypes exhibit clear transcriptomic variations across different cortical regions, interneuron

46 subtypes maintain a consistent profile independent of the cortical region examined[3]. Nonetheless, previous studies

47 demonstrated that interneurons form subtype-specific synaptic connections with particular excitatory neuron populations, a

48 preference observed across various regions of the cortex[4–10]. The ability of clonally-related interneurons to adopt different

49 identities and integrate precisely with distinct excitatory neurons present in specific cortical regions[11–15] implies a crucial

50 role for excitatory neurons in directing the development of interneuron subtypes. Our quantitative analysis of different

51 interneuron subtypes showed that interneuron subtypes in different cortical regions generally adapt to the composition of

52 local pyramidal neurons (PNs). To directly test the influence of PNs on interneuron diversity, we employed genetic strategies

53 to selectively alter the identity of specific PN types and demonstrated that the quantity of particular PVALB and SST

54 interneuron subtypes changed in accordance with this shift. Importantly, these changes occur through distinct mechanisms:

55 PNs promote the survival of their partner SST interneuron subtypes, while inducing fate changes in PVALB interneuron

56 populations towards their preferred subtypes.

57

58 **Interneuron subtypes exhibit consistent laminar distributions across cortical regions**

59 Cortical interneurons are categorized into five cardinal classes based on their expression of *Pvalb*, *Sst*, *Vip*, *Sncg*, or *Lamp5*

60 genes[1–3]. The PVALB and SST classes together constitute ~70% of total cortical interneurons, while the other three classes

61 make up the remainder. Despite recent advances in profiling the myriad cellular features of cortical interneurons, a

62 consensus on the finer subtypes within these cardinal classes has not been reached[16]. Based on single-nuclei RNA

63 sequencing (snRNA-seq) of postnatal day 28 (P28) mouse cortical interneurons[17], which we believe more accurately

64 captures the relative proportions of different interneurons than single-cell sequencing, we defined a total of 19 subtypes

65 within the PVALB and SST interneuron classes, naming them after the marker genes they express (Fig. 1a and Extended

66 Data Fig. 1a-b). An additional 15 subtypes were identified within the remaining three cardinal classes. However, due to

67 their smaller size and restricted distribution mostly in L2/3, this study primarily focuses on PVALB and SST interneurons

68 to better illustrate the principles discussed here.

69   To explore regional differences in the transcriptome of each interneuron subtype, we divided the snRNA-seq dataset

70 based on the cortical regions from which interneurons were collected. All subtypes were present in both the secondary motor

71   cortex (MOs) and the primary visual cortex (VISp), two regions located at the opposite ends of the anterior-posterior axis

72   of the brain. We then developed a computational method to quantitatively assess the transcriptomic differences across

73   regions that uses each cell's nearest neighborhood as a unit and compares the closest neighborhoods across two cortical

74   regions within an integrated transcriptomic dimensional space, assigning each cell a significance score (See Methods).

75   Consistent with previous studies[3], interneurons generally showed consistent transcriptomic profiles across both cortical

76   regions, with most PVALB interneurons showing no significant regional differences. Nonetheless, minor regional

77   transcriptomic variations were observed more prominently in SST interneurons than in PVALB interneurons (Extended

78   Data Fig. 1c). Analyzing each subtype revealed that one PVALB subtype (PVALB-Unc5b chandelier cells) and three SST

79   subtypes (SST-Crh-1, SST-Nmbr-1, SST-Chodl) differed significantly between the MOs and VISp regions, with more than

80   50% of cells showing significant regional differences (Extended Data Fig. 1d). The generally greater regional transcriptomic

81   variation in SST interneurons likely reflects their closer association with local PNs. Consequently, the larger transcriptomic

82   disparities in PNs across regions necessitate SST interneurons to fine-tune their gene transcription accordingly.

83   Utilizing the published adult mouse whole-brain multiplexed error-robust fluorescence *in situ* hybridization

84   (MERFISH) dataset[18], we examined the distribution patterns of these interneuron subtypes (Extended Data Fig. 2a). Each

85   subtype showed a laminar specific distribution that is consistent across different cortical regions (Fig. 1c-d, Extended Data

86   Fig. 3). In most cases, their spatial positioning correlates with the types of PN they are believed to target. For example,

87   PVALB-Rorb and SST-Hpse both show axonal projections that preferentially target layer 4 (L4)[4] (Extended Data Fig. 1f)

88   and are predominantly localized within or near L4. Additionally, both PVALB-Fzd6 and SST-Chrna2 (N.B. also referred

89   to as SST-Myh8[2,4], Extended Data Fig. 1b) are specifically situated in L5b. The former extend their axons laterally within

90   L5b (Extended Data Fig. 1g), while the latter project their axons to L1 but preferentially target the dendrites of L5b

91   pyramidal tract (PT) neurons[4,19]. These findings suggest that interneuron subtypes defined at this resolution anatomically

92   form stereotypical local microcircuitry with specific PN types.

93

94   **Interneuron subtype abundance parallel local pyramidal neuron types in different cortical regions.**

95   Although major types of PN are shared across the isocortex[2,3], their relative proportions vary significantly across different

96   cortical regions. The most distinct regional difference is exemplified by a notably expanded population of L4

97   intratelencephalic (IT) neurons in primary sensory cortices compared to non-sensory regions (L4 IT: 3% in MOs, 27% in

98   SSp, 19% in VISp) (Fig. 1e, Extended Data Fig. 2b). Interestingly, the proportion of interneuron subtypes in different

99   cortical regions appears to vary according to the abundance of the PN types they target. For instance, based on the MERFISH

100   dataset, while the overall density of SST interneurons remains comparable across different cortical regions[20], the proportion

101   of L4-targeting SST-Hpse more than doubles in sensory cortices compared to MOs (SST-Hpse: 8% in MOs, 25% in SSp,

102   19% in VISp). Similarly, the proportion of PT-targeting SST-Chrna2 interneurons[4,19] varies across different regions (SST-

103   Chrna2: 16% in MOs, 8% in SSp, 13% in VISp), aligning with the relative abundance of L5b PT neurons in each region

104   (L5 PT: 7% in MOs, 3% in SSp, 7% in VISp) (Fig. 1c,e). These regional variations are also evident in snRNA-seq data and

105   through genetic labeling of specific SST subtypes (Fig. 1b, Extended Data Fig. 1e, 2d-h). PVALB interneurons exhibit

106   similar regional differences, with L4-targeting PVALB-Rorb being more prevalent in sensory cortices (PVALB-Rorb: 3%

107   in MOs, 33% in SSp, 8% in VISp), while L5b PVALB-Fzd6 are more abundant in the motor cortex (PVALB-Fzd6: 18% in

108   MOs, 11% in SSp, 13% in VISp) (Fig. 1b,c,e, Extended Data Fig. 2b). Beyond these prominent differences, other

109   interneuron subtypes show more subtle regional variations, which nonetheless generally mirror the relative proportions of

110   PN types. For instance, the lower proportion of L6 interneurons in VISp, PVALB-Slc39a8 and SST-Nmbr-1/2, correlates

111   with a lower proportion of L6 IT neurons in VISp (Fig. 1e, Extended Data Fig. 1e). For a comprehensive overview, a

112   breakdown of the proportions of each interneuron subtypes present in every layer for MOs, SSp and VISp is provided

113   (Extended Data Fig. 2c). These findings reveal a close correspondence between interneuron subtypes and their associated

114   PN populations. This suggests that as the interneurons migrate into the cortex during development, their interactions with

115   local PN likely play a critical role in establishing the cell-type-specific microcircuitry observed in the adult cortex.

116

Pyramidal neuron identity controls interneuron subtype composition

118   Previous studies using various mutant models have shown that changes in PN identity can influence the overall laminar

119   distribution of interneurons and alter inhibitory synaptic properties[21–27]. To test how changes in PN identity impact the

120   precise relationship between specific pyramidal neuron and interneuron subtypes, we examined cortical interneurons in

121   *Fezf2* knockout (KO) mice. *Fezf2* is a key transcription factor for the specification of deep-layer PNs and is never expressed

122   within interneuron populations. Unlike other mutant models (e.g., *Reeler*, *Satb2* KO) where the transcriptomes of most PNs

123   are significantly affected, the loss of *Fezf2* results in a clear fate-switch of subcerebral projection neurons to callosal

124   projection neurons, offering a unique opportunity to study the changes in those interneuron subtypes that specifically

125   associated with the two impacted populations[22,28,29]. Consistent with previous reports, analysis of published snRNA-seq

126   data[30] revealed that the absence of *Fezf2* resulted in a complete loss of L5 near-projecting (NP) and PT neurons, two

127 populations that normally reside in L5b, and an increase in L6 IT neurons. Meanwhile, other pyramidal neuron types L4/5

128 IT, L5 IT, and L6 corticothalamic (CT) populations were mostly preserved albeit with altered transcriptomes (Fig. 2a-c,

129 Extended Data Fig. 4a-b). Using the *Dlx5/6-Cre* driver line to enrich for interneurons, we performed snRNA-seq on

130 interneurons from both control and *Fezf2* KO cortices of P20 mice. Interestingly, two interneuron subtypes located in L5b,

131 PVALB-Fzd and SST-Chrna2, showed an approximately 80% reduction in *Fezf2* KO cortex. Conversely, subtypes residing

132 in L6, including PVALB-Slc39a8, SST-Nmbr-1/2, showed an approximate two-fold increase in proportion (Fig. 2d-e).

133 Previous studies have shown that SST-Chrna2 preferentially innervates L5 PT, whereas SST-Nmbr-1/2 preferentially

134 innervates deep-layer IT neurons[4]. Hence, these changes match with the changes in the PN types in *Fezf2* mutant and the

135 expected connectivity of these interneuron subtypes. Additionally, there seems to be a paradoxical loss of L6 PVALB-Th

136 interneurons in the *Fezf2* mutant, which constitutes a small fraction in control (2% of total PVALB) and was not further

137 investigated in this study (Extended Data Fig. 4c-d).

138   To confirm these results, we conducted MERFISH and Slide-seq experiments, two orthogonal spatial transcriptomic

139 methods, to examine the number and distribution of deep-layer PVALB and SST interneurons in different cortical regions

140 of adult control and *Fezf2* KO mice (Fig. 2f; Extended Data Fig. 5a-e). These results further demonstrated the loss of L5b

141 and gain of L6 PVALB and SST interneurons in *Fezf2* mutants[22] that are observed across MOs, SSp and VISp regions (Fig.

142 2g). Moreover, the limited remaining PVALB-Fzd6 and SST-Chrna2 interneurons in *Fezf2* mutants showed a shifted

143 distribution towards L6, whereas the expanded populations of PVALB-Slc39a8 and SST-Nmbr-1/2 interneurons had a

144 broader distribution, although predominantly confined to the expanded L6 in the mutant cortex (Extended Data Fig. 5f).

145 These changes in the number and distribution of SST interneurons were further confirmed by the genetic labeling of SST-

146 Chrna2 subtype and RNAscope *in situ* hybridization against genetic markers for SST-Nmbr-1/2 subtypes in control and

147 *Fezf2* mutants (Extended Data Fig. 4g-h).

148   Previous studies have shown a shift in the overall laminar distribution of PVALB and SST interneurons towards

149 upper layers (L2/3, L4) in the *Fezf2* KO cortex [22]. Our results corroborate this observation (Extended Data Fig. 6a-b). A

150 close examination of the subtype composition in each cortical layer based on MERFISH data revealed that the increase in

151 upper layer interneurons appears to result from the redistribution of PVALB-Reln and SST-Hpse subtypes, without an

152 obvious change in their overall number (Extended Data Fig. 6c-f). Both subtypes normally reside above L6, so the expanded

153 L6 in *Fezf2* mutants likely generates a stronger repulsive signal that pushes these interneurons further into the upper layers.

154 This intriguing phenomenon merits further investigation, but it falls outside the primary focus of this study.

155   Analysis of transcriptomic changes in *Fezf2* mutants revealed that both PVALB-Fzd6 and SST-Chrna2 interneurons

156   lost many of their subtype-specific defining features under mutant conditions, likely due to improper maturation in the

157   absence of their normally associated PN types. Conversely, SST-Nmbr-1/2 interneurons acquired novel features in *Fezf2*

158   mutants (Extended Data Fig. 4e-f). Using viral genetic strategies to label these L6 SST interneurons, we observed that they

159   seemed to have more elongated dendrites along the cortical column, and fewer L1 axons in the mutant cortex compared to

160   the control (Extended Data Fig. 4i). These morphological changes likely reflect the transcriptomic alterations as an

161   adaptation to the expanded L6 in the *Fezf2* mutants. In contrast, L6 PVALB-Slc39a8 interneurons did not show significant

162   transcriptomic differences between control and mutant cortex. Akin to the lack of transcriptomic variation in PVALB

163   interneurons across different cortical regions, these results further suggest that PVALB interneurons are less sensitive to

164   subtle changes in the transcriptome of the PN types they are associated with, except for changes that affect PN identity.

165   In summary, our study of *Fezf2* mutants, which solely affect PN identity, revealed that PNs exert a non-autonomous,

166   subtype-specific influence on cortical interneurons. These findings demonstrate that the relative numbers and distributions

167   of different interneuron subtypes depend significantly on the specific PN subtypes to which they are ultimately connected.

168

169   **Preventing *Bax*-dependent apoptosis partially rescues the *Fezf2* mutant phenotype on cortical interneurons**

170   Previous studies have shown that ~40% of cortical interneurons undergo programmed cell death around P7-9, a process

171   modulated by PNs[31–33]. To directly test whether PNs influence the relative number of different interneuron subtypes by

172   modulating their survival, we prevented cell death in PVALB and SST interneurons by removing *Bax*, a key gene involved

173   in apoptosis of cortical interneurons, using *Nkx2.1-Cre*;*Bax$^{fl/fl}$*. To confirm the effects of *Bax* removal, we quantified

174   genetically labeled cortical interneurons in control (*Nkx2.1-Cre*;*Bax$^{fl/+}$*;*Rosa26$^{LSL-h2b-GFP}$*) and *Bax* cKO (*Nkx2.1-*

175   *Cre*;*Bax$^{fl/fl}$*;*Rosa26$^{LSL-h2b-GFP}$*) mice and observed a 36% increase in the total amount of labeled interneurons in *Bax* mutants

176   (Extended Data Fig. 7c-d). Specifically, RNAscope *in situ* hybridization experiments showed a 22% increase of PVALB

177   interneurons and a 31% increase of SST interneurons in *Bax* cKO, without affecting their laminar distribution (Fig. 3a,

178   Extended Data Fig. 7b,e-f). Consistent with previous reports suggesting no significant increase in interneuron cell death in

179   *Fezf2* mutant[22], *Fezf2* KO_*Bax* cKO mice (*Nkx2.1-Cre*;*Fezf2$^{lacZ/lacZ}$*;*Bax$^{fl/fl}$*) showed a 22% increase in PVALB interneurons

180   and a 32% increase in SST interneurons compared to *Fezf2* KO mice, mirroring the increase observed in control mice (Fig.

181   3a, Extended Data Fig. 7g).

182 To compare the effects of *Bax* removal on the composition of cortical interneurons in both control and *Fezf2* mutant

183 conditions, we performed snRNA-seq of PVALB and SST interneurons from control, *Bax* cKO, *Fezf2* KO, and *Fezf2*

184 KO_*Bax* cKO mice at P14, an age when apoptosis in interneurons has concluded in the control condition. In both *Bax* cKO

185 conditions, we observed two clusters, constituting ~10% of the total interneurons in the dataset, that were absent in both the

186 control and *Fezf2* KO conditions. These *Bax* cKO-specific interneurons expressed genes typically found in interneurons

187 outside the cortex (Extended Data Fig. 7h-i), suggesting they are likely misguided interneurons, and were not further

188 analyzed. The remaining interneurons across all four conditions aligned and integrated well (Fig. 3b). To account for a

189 potential increased variability in *Bax* cKO samples, we included two biological replicates for both *Bax* cKO and *Fezf2*

190 KO_*Bax* cKO conditions, and the results seemed consistent across replicates (Extended Data Fig. 7j). We then compared

191 the proportions of different interneuron subtypes across different conditions. The proportions of interneurons in *Bax* cKO

192 appeared comparable to control conditions, suggesting that a similar proportion of cell death occurs for each interneuron

193 subtype during development. Interestingly, *Bax* cKO in the *Fezf2* mutant background partially rescued the loss of SST-

194 Chrna2 but not PVALB-Fzd6 (Fig. 3c).

195 To confirm these results, we performed MERFISH and Slide-seq experiments across four conditions at P14 in adult

196 mouse SSp cortices (Fig. 3d, Extended Data Fig. 8a,f). Previous studies suggested that interneuron numbers and distribution

197 stabilize after P14[20]. As such, data from both ages were combined to increase statistical power. Additionally, no obvious

198 differences were noted between *Fezf2* wild-type (WT) and *Fezf2* heterozygous (HET), or between *Fezf2* KO and *Fezf2*

199 KO_*Bax* cHET (Extended Data Fig. 8d). Therefore, our control dataset included both wild-type and heterozygous alleles.

200 Note that the *Nkx2.1-Cre* allele labels the majority of deep-layer PVALB and SST interneurons, but misses ~40-50% of

201 those in the superficial layers[34] (Extended Data Fig. 7a). Nevertheless, as the analysis involving *Bax* cKO conditions were

202 focused on interneurons found in deep layers (L5-6), the lack of labeling in superficial layers is not relevant. Consistent

203 with snRNA-seq results, *Bax* cKO in control conditions does not largely alter the proportion of interneuron subtypes, except

204 for PVALB-Fzd6, which increased slightly from 8% in control to 12% in *Bax* cKO (Fig. 3e, Extended Data Fig. 8e). Notably,

205 removing *Bax* in *Fezf2* mutants does not rescue the reduced proportion of PVALB-Fzd6 compared to control, while the

206 proportion of SST-Chrna2 doubled in *Fezf2* KO_*Bax* cKO condition, reaching a level comparable to the control condition

207 (Fig. 3e). More precisely, comparing the number of individual subtypes by normalizing to deep-layer PN numbers also

208 showed a two-fold increase in the number of SST-Chrna2 interneurons in *Fezf2* KO_*Bax* cKO, whereas other subtypes

209 remain unchanged with or without *Bax* in *Fezf2* mutants (Fig. 3f, Extended Data Fig. 8b).

210   Taken together, these results suggest that the loss of SST-Chrna2 in *Fezf2* mutants is due to increased apoptosis in

211   this subtype, although the exact cause remains unclear. It is possible that without their associated PNs, SST-Chrna2

212   interneurons fail to mature properly or exhibit decreased activity, both of which could lead to programmed cell death. In

213   contrast, the loss of PVALB-Fzd6 appears to be independent of cell death. This suggests that PNs may directly influence

214   the differentiation of PVALB subtypes, causing PVALB-Fzd6 to transform into PVALB-Slc39a8 in *Fezf2* mutants.

215

216   **Pyramidal neurons direct PVALB subtype differentiation and promote SST subtype maturation**

217   To find evidence for the transformation of L5b into L6 PVALB interneurons in *Fezf2* mutants, and to further elucidate the

218   cause of increased cell death of SST-Chrna2 interneurons under such conditions, we performed snRNA-seq on cortical

219   interneurons from control and *Fezf2* KO mice at P7. Characterizing them at the onset of programmed cell death allowed us

220   to capture PVALB-Fzd6 in the process of transforming into PVALB-Slc39a8 and to examine the status of SST-Chrna2

221   interneurons as they begin to undergo apoptosis in *Fezf2* KO cortices. Even though a decrease in the number of both

222   PVALB-Fzd6 and SST-Chrna2 interneurons was already apparent at P7 in *Fezf2* KOs (Extended Data Fig. 9d-e), these

223   populations were sufficiently large at this age to allow for meaningful analysis before their numbers declined further.

224   To predict how the transcriptome of each subtype will evolve developmentally, we conducted RNA velocity[35]

225   analysis on P7 snRNA-seq data. This analysis leverages the variations in gene expression profiles of individual cells within

226   each subtype, which likely reflect their varying positions along the developmental trajectory, to forecast the direction of

227   overall transcriptomic changes. Interestingly, while PVALB-Fzd6 and PVALB-Slc39a8 interneurons in the control dataset

228   are predicted to become more distinct from each other, a major fraction of PVALB-Fzd6 interneurons in *Fezf2* mutants

229   appear to be transitioning towards PVALB-Slc39a8 identity (Fig. 4a). In comparison, SST-Chrna2 did not show a clear

230   trend towards SST-Nmbr-1/2 in either condition (Extended Data Fig. 9f). Using the control data as a reference, we identified

231   marker gene sets (ID genes) that are differentially expressed between PVALB-Fzd6 and PVALB-Slc39a8, as well as

232   between SST-Chrna2 and SST-Nmbr1/2 subtypes. Aligned with a fate switch of PVALB-Fzd6 interneurons, the expression

233   of PVALB-Fzd6 ID genes is significantly reduced, with an increase in the expression of PVALB-Slc39a8 ID genes in these

234   cells in *Fezf2* mutants (Fig. 4b). In contrast, SST-Chrna2 ID genes were retained in SST-Chrna2 interneurons in *Fezf2*

235   mutants, although there was also an increased expression of genes preferentially expressed in SST-Nmbr-1/2 interneurons

236   (Extended Data Fig. 9j). A closer examination showed that ~50% of the acquired SST-Nmbr-1/2 features in SST-Chrna2

237   interneurons in *Fezf2* mutants were common signatures shared between L6 PVALB and SST interneurons (Extended Data

238   Fig. 10), likely caused by the shifted distribution of these interneurons into L6 and their adaptation to the altered local

239   environment in *Fezf2* KOs.

240   As PVALB-Fzd6 interneurons in *Fezf2* mutants lose some of their defining features, we reasoned that they might

241   remain immature without their normal synaptic partners. To test this, we compared PVALB-Fzd6 interneurons in *Fezf2*

242   mutants at P7 to PVALB-Fzd6 in control at P2. Although not all interneuron subtypes can be confidently identified at P2 in

243   control mice, both PVALB-Fzd6 and SST-Chrna2 are among the earliest subtypes to mature and therefore can be clearly

244   identified at this age. Indeed, marker genes identified at P7 are already specifically expressed in these two subtypes by P2

245   (Extended Data Fig. 9g-i). Moreover, cross-age comparison revealed that PVALB-Fzd6 interneurons in the mutant condition

246   retain significantly higher expression of features characteristic of an earlier developmental age (Fig. 4b). Their overall

247   transcriptomic profile resembles P2 PVALB-Fzd6 more than P7 in control mice (Fig. 4c). In comparison, while SST-Chrna2

248   interneurons also showed increased immature features at P7 in *Fezf2* mutants, their overall transcriptomic profile was closer

249   to P7 controls than P2 (Extended Data Fig. 9j-k). Finally, despite changes in PN identity in *Fezf2* mutants are already

250   obvious at P1 (Extended Data Fig. 9a-c), there is no significant loss of either PVALB-Fzd6 and SST-Chrna2 interneurons

251   in *Fezf2* mutants at P2, based on both snRNA-seq and MERFISH data (Fig. 4d). This suggests that changes in interneuron

252   subtype composition in *Fezf2* mutants occur after migrating interneurons invade the cortex and interact with PNs.

253   Taken together, these data suggest that the loss of L5b and gain of L6 PNs in *Fezf2* mutants induce corresponding

254   changes in interneuron subtypes through two distinct mechanisms (Figure 5). While SST interneuron subtypes change their

255   relative numbers through selective apoptosis, PVALB interneurons appear to be able to transform from one subtype to

256   another in response to the changes in pyramidal cell identity in *Fezf2* mutants.

257

258   **Discussion**

259   Previous work from our laboratory[4] and others[5–9] have revealed a close association between specific PN and interneuron

260   types, forming stereotyped cortical microcircuits that are shared across various cortical regions. It is imperative to

261   understand how this precise circuitry is established during development. Based on previous studies and our analysis, we

262   believe that interneurons enter the cortex already seeded to become specific subtypes, as dictated by their intrinsic gene

263   regulatory networks (GRNs). Upon entering the cortex, these interneurons interact with local pyramidal neurons, receiving

264   external signals that modulate their maturation and adjust the relative abundance of different interneuron subtypes.

265   Importantly, such interactions are subtype-specific, ensuring an inhibitory network that aligns with the composition of local

266 pyramidal neuron types. While the mechanisms for adjusting the subtype proportion of PVALB and SST interneurons

267 appear different, we believe that they reflect the same underlying principles influenced by their distinct maturation rates.

268 Although PVALB and SST interneurons are born around the same time, SST interneurons rapidly establish their adult

269 identities and begin functioning shortly after arriving in the cortex, while PVALB interneurons mature much later[36–39]. Due

270 to these intrinsic differences in their developmental timetable, the GRNs that define SST subtype identity become relatively

271 fixed as they integrate with PNs, while those for PVALB interneurons remain plastic during early postnatal stages. As a

272 result, in the *Fezf2* mutants, most SST-Chrna2 fail to mature properly in the absence of their synaptic PN partners and

273 undergo programmed cell death. In contrast, the GRNs for PVALB subtypes remain sufficiently flexible to allow the

274 transformation of their identity to the altered balance of PNs in *Fezf2* mutants. However, the few SST-Chrna2 cells that

275 survive tend to shift into L6 and acquire genetic features, accordingly, suggesting that the GRNs of SST interneurons are

276 not entirely rigid. Thus, PVALB and SST interneurons exemplify two extremes in how their intrinsic GRN programs are

277 influenced by extrinsic signals that establish their identities and abundance. This dynamic interplay highlights the nuanced

278 mechanisms that selectively guide interneuron development and their integration into cortical circuits.

279

280
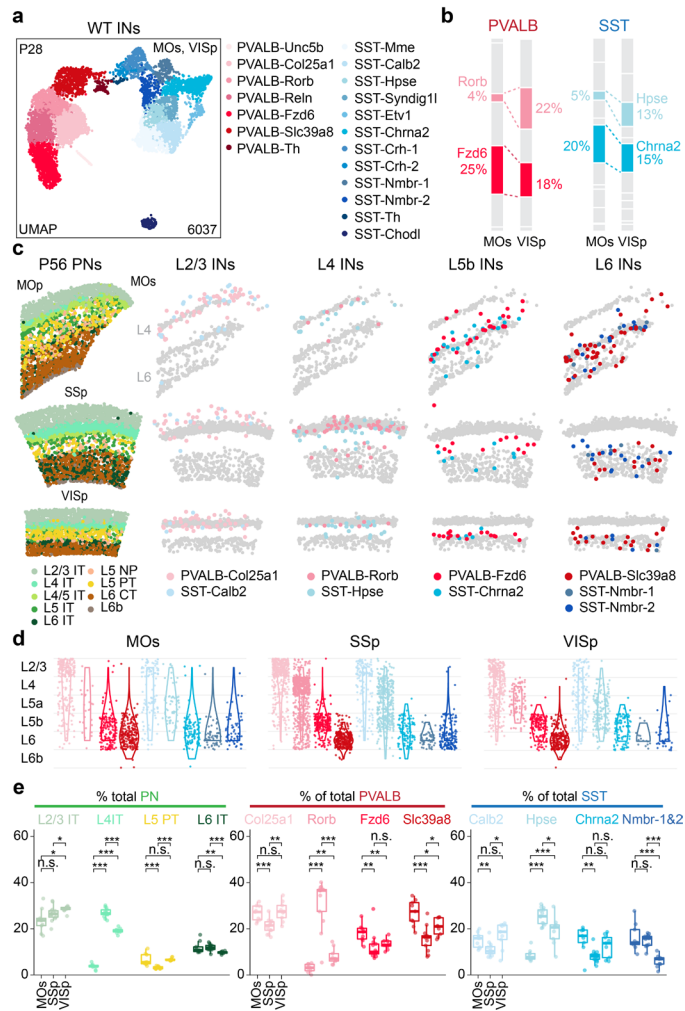
Figures

Figure 1. PVALB and SST interneuron subtypes show stereotyped laminar distribution and regional-specific changes in proportion.

a, Uniform manifold approximation and projection (UMAP) of snRNA-seq data on genetically labeled cortical interneurons of P28 *Dlx5/6-Cre;Rosa26[LSL-h2b-GFP]* mice, depicting 7 PVALB subtypes and 12 SST subtypes. Data was collected from both MOs (ALM) and VISp regions[17]. **b,** Proportions of individual subtypes within the total PVALB or SST population based on snRNA-seq data, compared between two sampled regions. **c,** Representative MERFISH spatial map of coronal brain sections of a P56 mouse from published datasets[18], illustrating the distribution of different pyramidal neurons (PNs) and selected interneuron subtypes across three cortical regions. **d,** Violin plots showing the laminar distribution of selected PVALB and SST interneuron subtypes in MOs (n=9 ROIs), SSp (n=13 ROIs), and VISp (n=9 ROIs) regions based on MERFISH data. **e,** Boxplots illustrating the proportion of selected PN, PVALB, and SST subtypes found in each cortical region. Wilcoxon rank-sum test without correction for multiple comparisons, n.s. not significant, p≥0.05; *p<0.05; **p<0.01; ***p<0.001. Detailed p-values are provided in Supplementary Table 2.

295
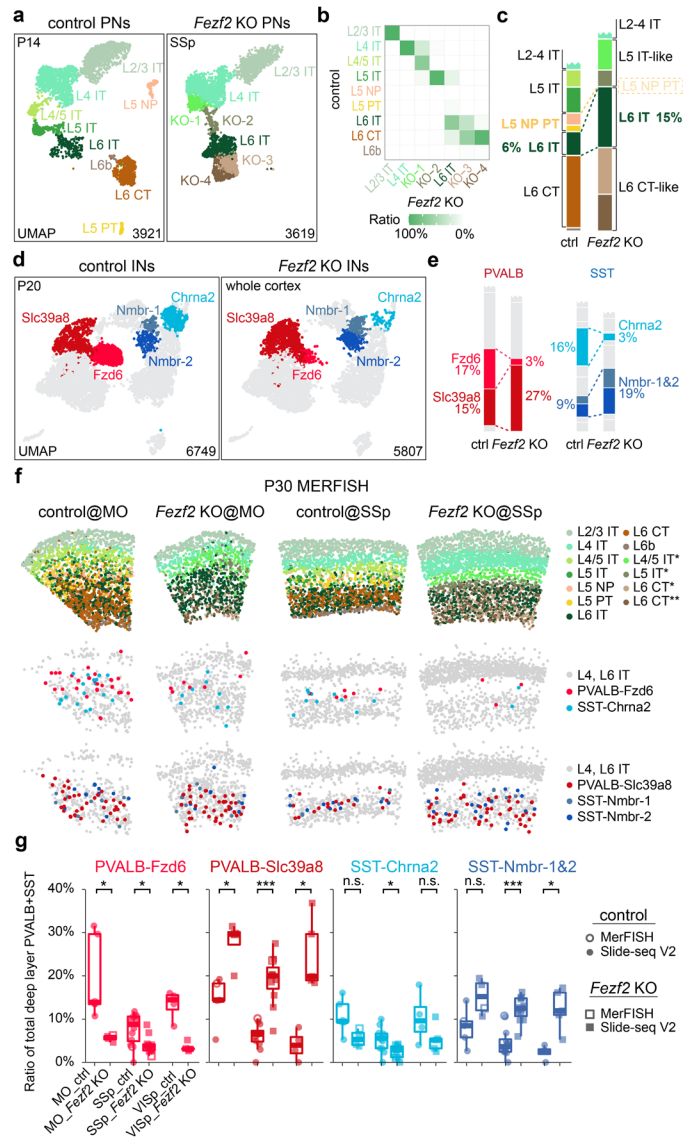
Figure 2. *Fezf2* KO changes the proportion of deep-layer PVALB and SST interneuron subtypes.

a, UMAP visualization of published snRNA-seq data of excitatory neurons from P14 control (*Fezf2* HET) and *Fezf2* KO

mouse SSp cortices[30]. **b,** Heatmap illustrating the correspondence of each PN type between control and *Fezf2* KO based

on transcriptomic similarity. KO-1 through KO-4 have been named as L4/5 IT*, L5 IT*, L6 CT*, and L6 CT** thereafter

to reflect their mapped identity. **c,** Proportion of deep-layer PNs in snRNA-seq data of control and *Fezf2* KO cortices. **d,**

UMAP visualization of snRNA-seq data on cortical interneurons from P20 control (*Dlx5/6-Cre;Rosa26$^{LSL-h2b-GFP}$*) and

Fezf2 KO (*Dlx5/6-Cre;Fezf2$^{lacZ/lacZ}$;Rosa26$^{LSL-h2b-GFP}$*) mice, highlighting five deep-layer interneuron subtypes with altered

proportions in the *Fezf2* mutant. **e,** Proportion of PVALB and SST interneuron subtypes in control and *Fezf2* KO cortices

based on snRNA-seq data, with selected subtypes highlighted. **f,** MERFISH spatial map of coronal brain sections from

MO and SSp cortices of P30 control and *Fezf2* KO mice, illustrating the distribution of PNs and selected interneuron

subtypes. **g,** Boxplot showing the proportion of selective PVALB and SST interneuron subtypes within all PVALB and

307   SST interneurons found in L5/6, based on both MERFISH and Slide-seq data. MO_ctrl: n=5 ROIs (1 MERFISH), n=4

308   mice; MO_*Fezf2* KO: n=4 ROIs (1 MERFISH), n=4 mice; SSp_ctrl: n=12 ROIs (1 MERFISH), n=8 mice (including 2

309   mice that are *Fezf2* HET_*Bax* cHET); SSp_*Fezf2* KO: n=11 ROIs (1 MERFISH), n=8 mice (including 2 mice that are

310   *Fezf2* KO_*Bax* cHET); VISp_ctrl: n=4 ROIs, n=4 mice; VISp_*Fezf2* KO: n=5 ROIs, n=2 mice. Age range for all samples:

311   4-6 weeks (including one published Slide-seq data[40]: puck 200306_02). Wilcoxon rank-sum test, n.s. not significant, p$\geq$

312   0.05; *p<0.05; **p<0.01; ***p<0.001. Detailed p-values are provided in Supplementary Table 2.
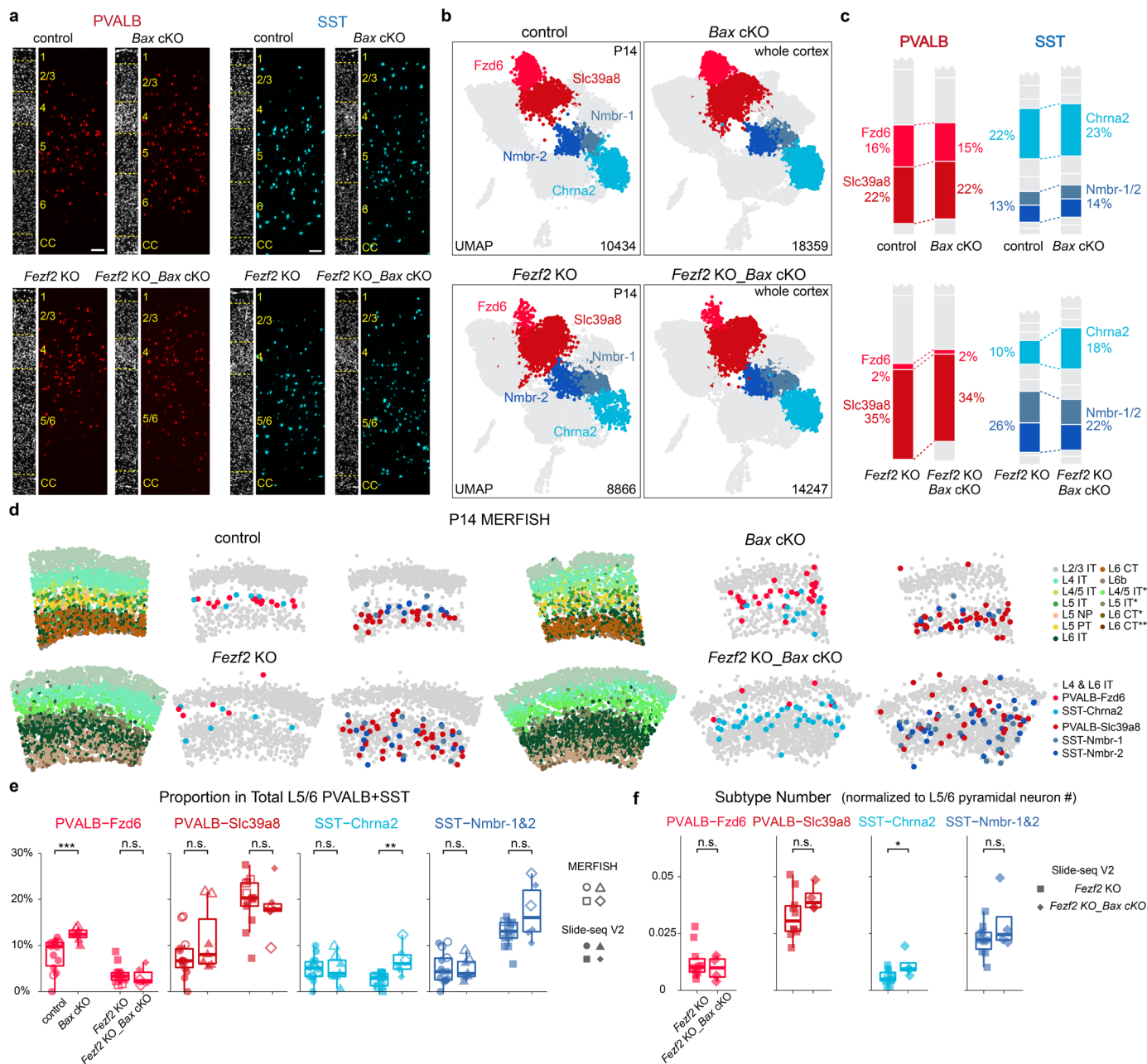
Figure 3. Preventing cell death rescues the loss of SST-Chrna2 but not PVALB-Fzd6 interneurons in *Fezf2* mutants.

a, Representative RNAscope *in situ* hybridization images showing labeled *Pvalb* and *Sst* mRNA transcripts in the SSp region of P28-33 mice with four different genotypes. DAPI counterstaining is provided on the left of each image for laminar distribution reference. Scale bar: 100 µm. **b,** UMAP visualization of snRNA-seq of sorted interneurons from control (*Nkx2.1-Cre;Bax^{fl/+};Rosa26^{LSL-h2b-GFP}*), *Bax* cKO (*Nkx2.1-Cre;Bax^{fl/fl};Rosa26^{LSL-h2b-GFP}*), *Fezf2* KO (*Nkx2.1-Cre;Fezf2^{lacZ/lacZ};Rosa26^{LSL-h2b-GFP}*), and *Fezf2* KO_*Bax* cKO (*Nkx2.1-Cre;Fezf2^{lacZ/lacZ};Bax^{fl/fl};Rosa26^{LSL-h2b-GFP}*) mice at P14. control: n=1, *Bax* cKO: n=2, *Fezf2* KO: n=1, *Fezf2* KO_*Bax* cKO: n=4 mice. **c,** Proportion of deep-layer PVALB and SST interneuron subtypes in snRNA-seq dataset. **d,** MERFISH spatial map of coronal brain sections from SSp region

323   of P14 mice of the four genotypes, showing PN and selected interneuron subtypes. **e,** Proportion of selected PVALB and

324   SST interneuron subtypes within all PVALB+SST interneurons found in L5/6, based on spatial transcriptomic data in the

325   SSp region. Control: n=14 ROIs (3 MERFISH), n=10 mice (WT: n=7, *Bax* cHET: n=1, *Fezf2* HET_*Bax* cHET: n=2); *Bax*

326   cKO: n=7 ROIs (2 MERIFSH), n=4 mice (all *Fezf2* HET_*Bax* cKO); *Fezf2* KO: n=13 ROIs (3 MERFISH), n=10 mice

327   (*Fezf2* KO: n=7, *Fezf2* KO_*Bax* cHET: n=3); *Fezf2* KO_*Bax* cKO: n=6 ROIs (2 MERFISH), n=4 mice. Age range: P14-

328   37, with one *Fezf2* KO mouse at 6-weeks old. **f,** Number of selected PVALB and SST subtypes normalized to the number

329   of deep-layer PNs based on Slide-seq data. *Fezf2* KO: n=10 ROIs, n=7 mice (*Fezf2* KO: n=5, *Fezf2* KO_*Bax* cHET: n=2);

330   *Fezf2* KO_*Bax* cKO: n=4 ROIs, n=3 mice. Wilcoxon rank-sum test, n.s. not significant, $p \geq 0.05$; *$p < 0.05$; **$p < 0.01$;

331   ***$p < 0.001$. Detailed p-values are provided in Supplementary Table 2.

332
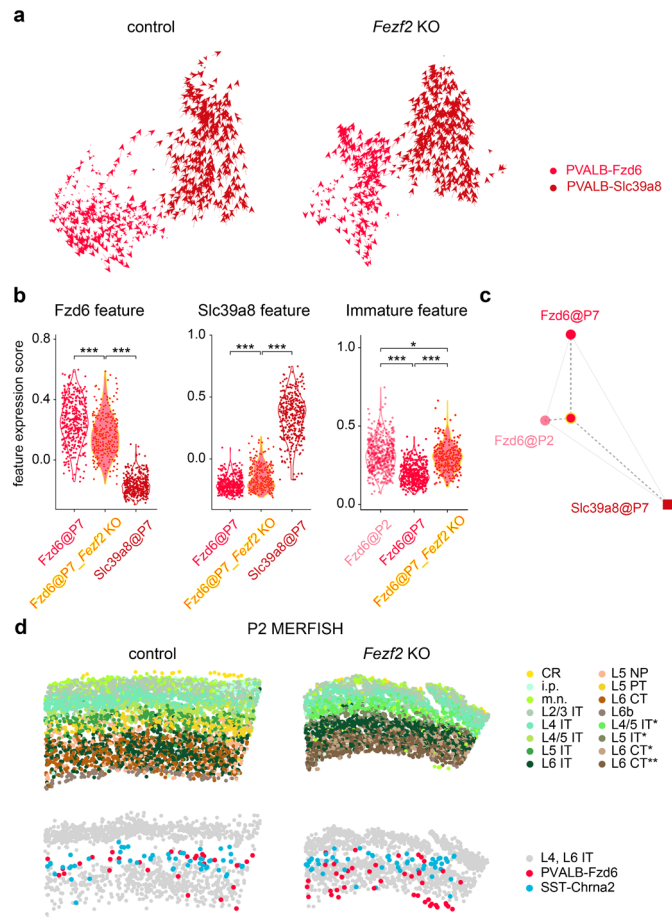
Figure 4. PVALB and SST interneurons in *Fezf2* mutants at early postnatal ages

a, RNA velocity analysis of snRNA-seq data on cortical interneurons collected from P7 control (*Fezf2* HET) and *Fezf2* KO mouse brains, showing gene expression dynamics of PVALB-Fzd6 and PVALB-Slc39a8 interneurons. **b,** The expression score of gene sets characteristic of PVALB-Fzd6, PVALB-Slc39a8 at P7, and PVALB-Fzd6 at P2 (referred to as Fzd6 feature, Slc39a8 feature, and immature features, respectively; see Methods) were compared between different groups of PVALB interneurons. This comparison demonstrates changes in the expression of these gene features in PVALB-Fzd6 interneurons in *Fezf2* mutants at P7. Wilcoxon rank-sum test, *p<0.05; **p<0.01; ***p<0.001. Detailed p-values are provided in Supplementary Table 2. **c,** Triangular Affinity Map of PVALB-Fzd6 interneurons in *Fezf2* mutants at P7 (see Methods), depicting the relative transcriptomic similarities among PVALB-Fzd6, PVALB-Slc39a8 at P7, and PVALB-Fzd6 at P2. **d,** MERFISH spatial map of coronal brain sections from the SSp region of control (*Nkx2.1-Cre;Fezf2^{lacZ/+};Bax^{fl/+}*) and *Fezf2* KO (*Fezf2^{lacZ/lacZ};Bax^{fl/fl}*) mice at P2, showing PN and selected interneuron subtypes. CR, Cajal-Retzius cells; i.p., intermediate progenitor; m.n., migrating neurons.
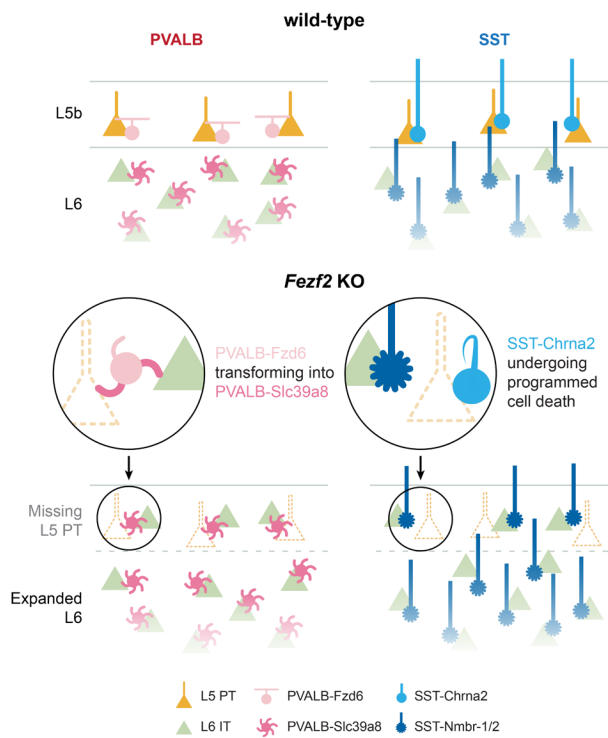
Figure 5. Schematic illustration of how PVALB and SST interneurons adapt to the changes in pyramidal neurons in *Fezf2* mutants.
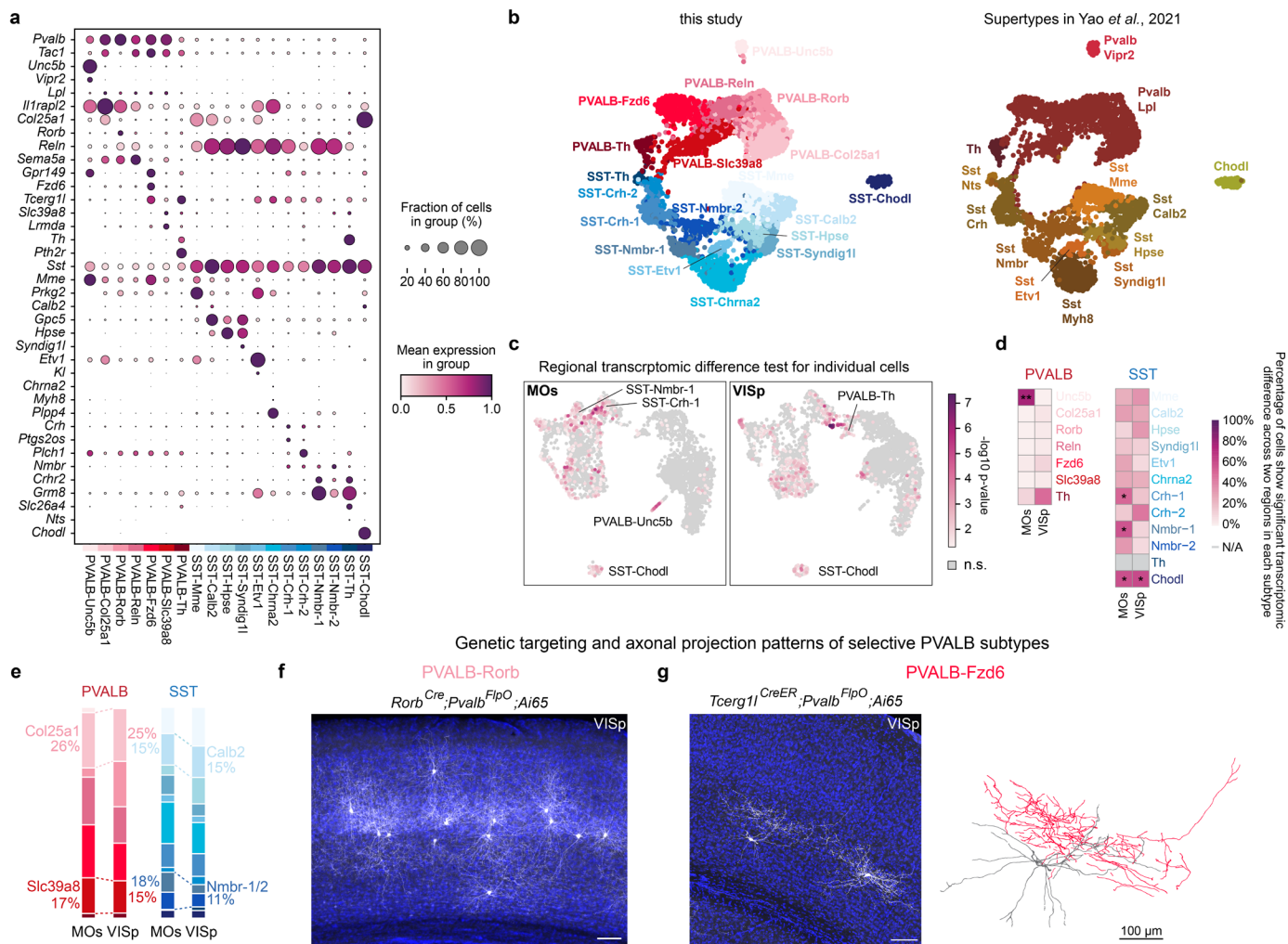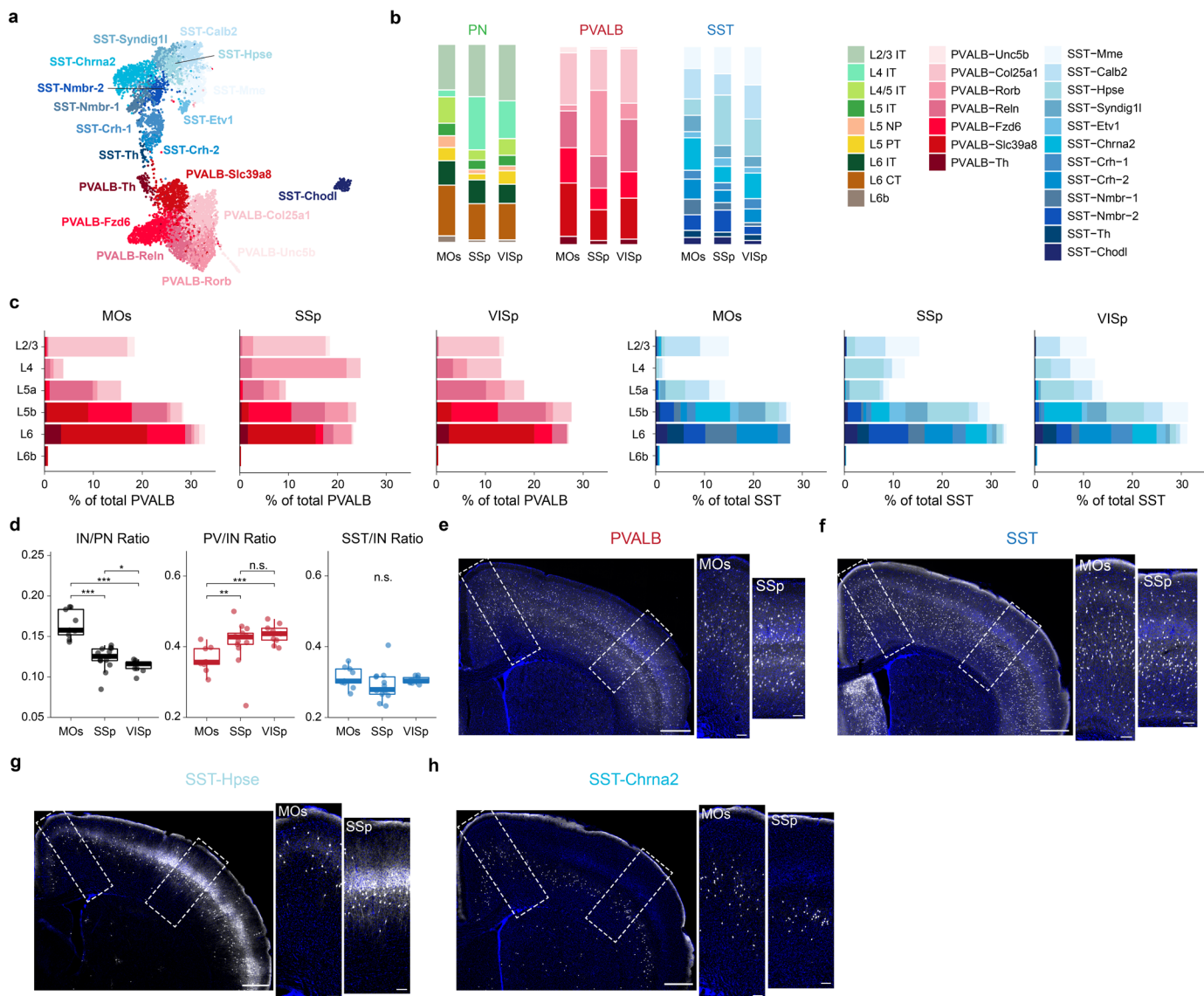
Extended Data Fig. 1 Features of PVALB and SST interneuron subtypes and regional-specific transcriptomic differences.

a, Dot plot showing the expression of marker genes for each PVALB and SST interneuron subtype. **b,** Analysis of published data showing the correspondence between subtypes identified in this study and supertypes defined in a previous publication[2]. **c,** Transcriptomic differences of PVALB and SST interneuron between MOs and VISp regions were assessed by Emergene (See Methods), which calculates a p-value reflecting the enrichment of region-specific gene signatures for individual nuclei, via a permutation test. n.s., not significant. **d,** Heatmap showing the percentage of cells within each cluster that exhibited significant regional differences. Cell types with ≥ 50% of cells showing regional significance were annotated with the p-value at the 50th percentile for each cell type as calculated by Emergene (*p<0.05; **p< 0.01). N/A: not analyzed, cluster size <10 cells. Detailed p-values are provided in Supplemental Table 2. **e,** Same bar plot as in Fig. 1b, now fully colored to indicate all subtypes. **f,** Intersectional genetic strategy preferentially targeting PVALB-Rorb interneurons, showing their axons concentrated in L4. Note that this strategy also labels some L5 PNs in SSp. **g,** Intersectional genetic strategy preferentially targeting PVALB-Fzd6 interneurons, showing that these interneurons

366   reside in L5b and extend their axons laterally within L5b. Sparse labeling can be achieved via low dose of tamoxifen

367   administration, allowing for the reconstruction of PVALB-Fzd6 interneuron morphology, with one example shown to the

368   right. Note that this strategy also labels L5 PT neurons in SSp. Scale bars: 100 μm.

369

Extended Data Fig. 2 Regional differences in the proportion of different PVALB and SST interneuron subtypes.

a, UMAP of P28 snRNA-seq data shown in Fig. 1a, now based on genes included in the MERFISH probe set,

demonstrating that these interneuron subtypes can be identified based on this 500 gene set. **b,** Proportion of PN, PVALB,

SST interneuron subtypes in different cortical regions based on MERFISH data. **c,** Bar plots showing the composition of

PVALB and SST interneuron subtypes in different cortical layers across three cortical regions. **d,** Boxplots comparing

interneuron (IN) to PN ratio, the ratio of PVALB interneurons in total interneurons, and the ratio of SST interneurons in

total interneurons in different cortical regions. Wilcoxon rank-sum test, n.s. not significant, $p \geq 0.05$; *$p < 0.05$; **$p < 0.01$;

***$p < 0.001$. Detailed p-values are provided in Supplemental Table 2. **e,** Coronal brain section of a P26 mouse

immunolabeled for PV (white) and counterstained by DAPI (blue). Scale bar: 500 μm. Higher magnification images of the

two different cortical regions outlined are shown to the right. Scale bar: 100 μm. **f-h,** Same arrangement as in (**e**), showing

genetically label SST interneurons and SST interneuron subtypes. **f,** All SST labeled in a P26 $Sst^{Cre};Sst^{FlpO};Ai65$ mouse; **g,**

381   SST-Hpse labeled in a P43 *Pdyn^{Cre};Npy^{FlpO};Ai65* mouse. Note that this strategy labels some SST-Calb2 interneurons; **h,**

382   SST-Chrna2 labeled in a P35 *Chrna2-Cre;Ai14* mouse.

383
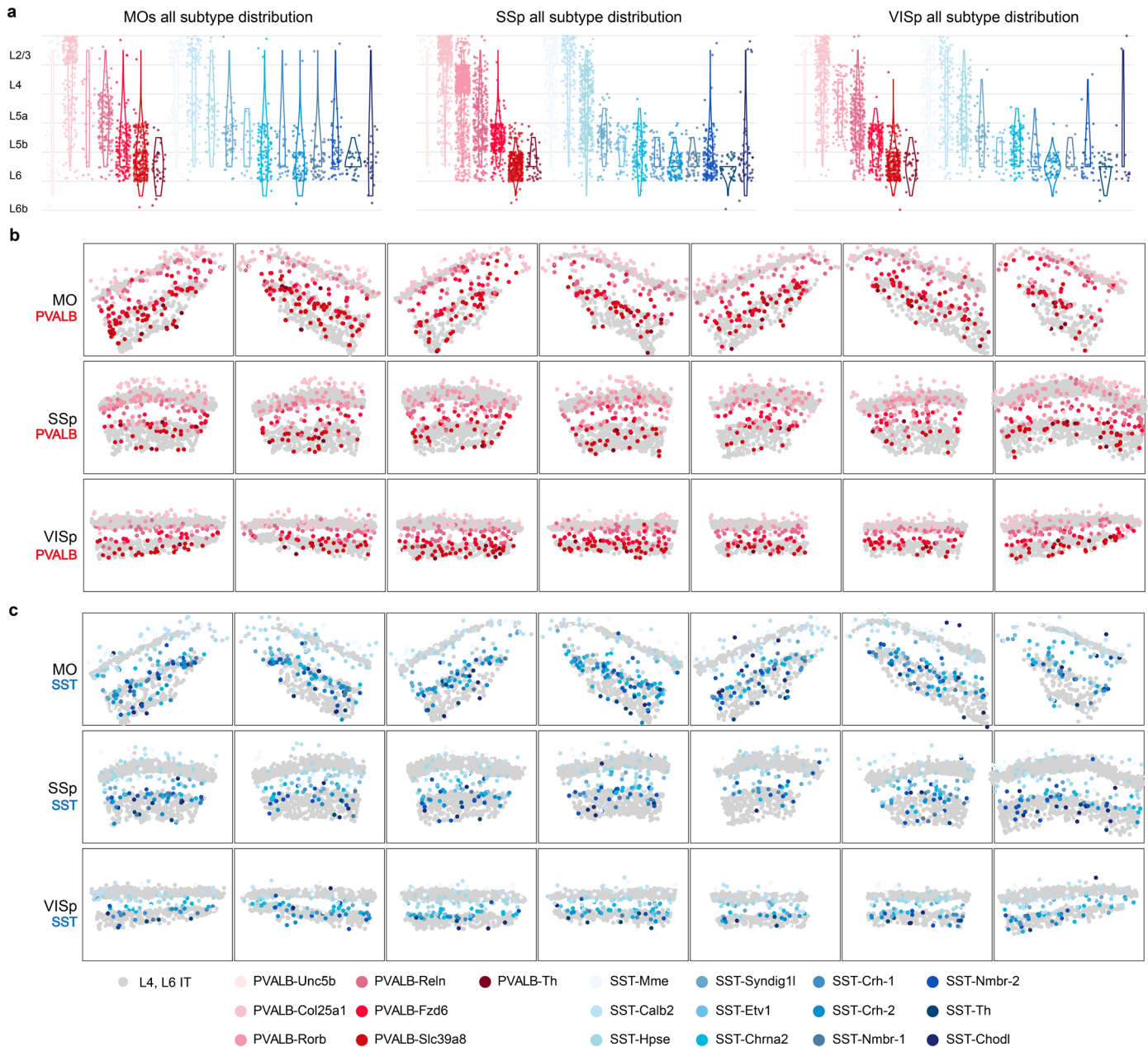
Extended Data Fig. 3 Gallery of MERFISH datasets showing the distribution of PVALB and SST interneuron subtypes.

a, Violin plots as in Fig. 1d, now showing the distribution of all PVALB and SST subtypes across three cortical regions.

b-c, Gallery of MERFISH spatial maps of different brain sections showing all identified PVALB and SST interneurons.
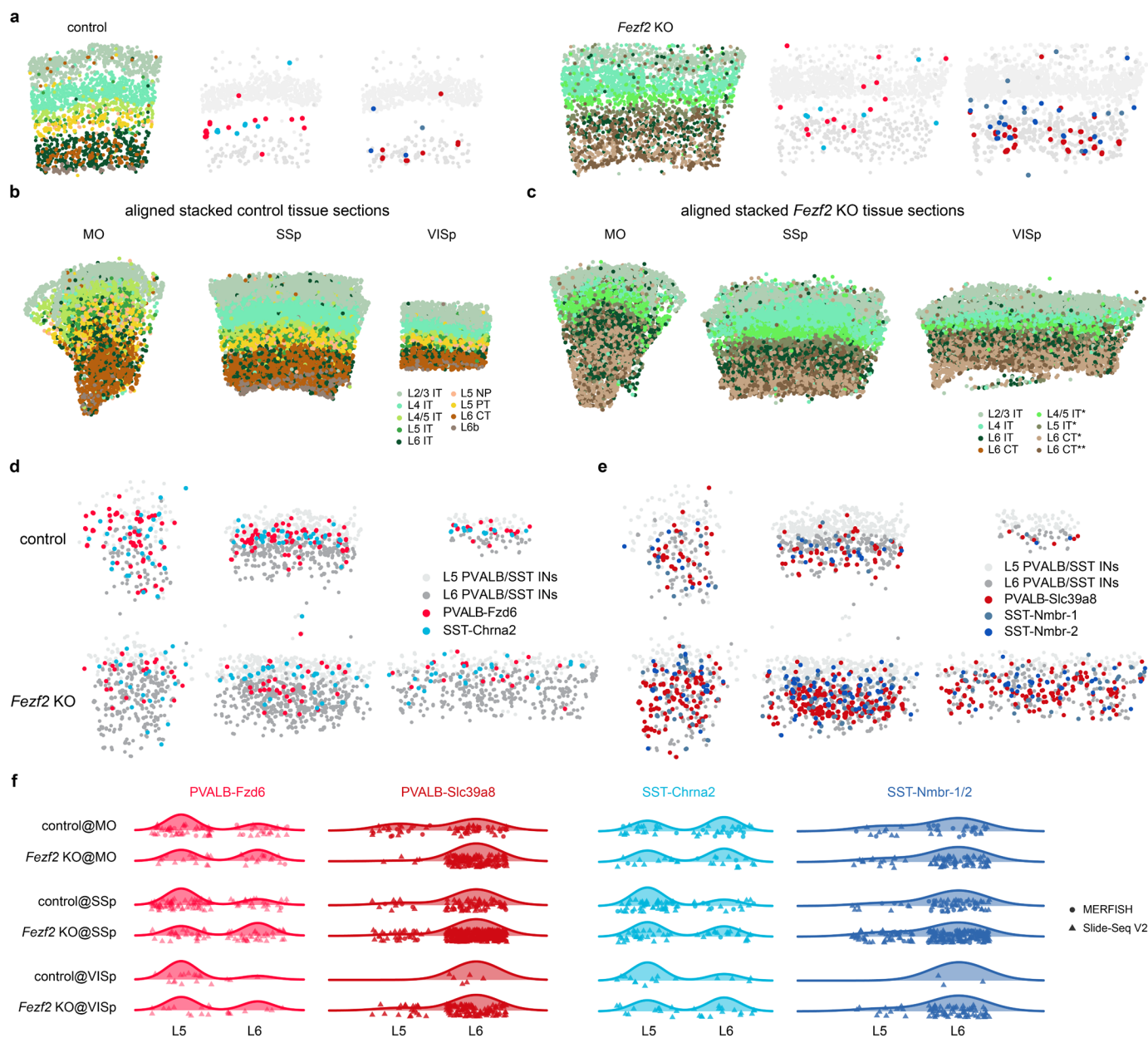
Extended Data Fig. 4 Change of cortical interneurons in *Fezf2* mutants.

a, Dot plot showing the expression of marker genes for different PN subtypes found in control and *Fezf2* KO cortices. **b,** Bar plot as in Fig. 2c, now showing the proportion of all PN subtypes. **c,** UMAP plot as in Fig. 2d, now highlighting all subtypes that exhibited either transcriptomic or proportional changes in *Fezf2* mutants. **d,** Bar plot as in Fig. 2e, now highlighting other subtypes that show changes in *Fezf2* mutants. **e,** Transcriptomic differences of PVALB and SST interneuron between control and *Fezf2* KO conditions were assessed by Emergene (See Methods), which calculates a p-value reflecting the enrichment of genotype-specific gene signatures for individual nuclei, via a permutation test. n.s., not significant. **f,** Heatmap showing the percentage of cells within each cluster that exhibited significant regional differences. Cell types with ≥ 50% of cells showing significance between two conditions were annotated with the p-value at the 50th percentile for each cell type, as calculated by Emergene (*p<0.05; **p< 0.01). N/A: not analyzed, cluster size <10 cells. Detailed p-values are provided in Supplemental Table 2. **g,** Representative images of genetically labeled SST-Chrna2 in different cortical regions of control (*Chrna2-Cre;Fezf2^{lacZ/+};Ai14*) and *Fezf2* mutant (*Chrna2-Cre;Fezf2^{lacZ/lacZ};Ai14*) mice

403   at P29. Scale bar: 100 μm. **h,** Representative RNAscope *in situ* hybridization images showing *Nmbr* and *Crhr2* mRNA

404   transcripts, two marker genes for SST-Nmbr-1 and SST-Nmbr-2 subtypes, in control and *Fezf2* KO mice at P28. Scale

405   bar: 100 μm. **i,** Representative images of labeled SST-Nmbr-1/2 interneurons in control and *Fezf2* mutants at P46. AAV-

406   PHP.eB-hDlx-DIO-ChR2-mCherry virus was introduced to SSp of control (*Crhr2^{Cre};Fezf2$^{lacZ/+}$*) and *Fezf2* mutant

407   (*Crhr2^{Cre};Fezf2$^{lacZ/lacZ}$*) mice via stereotaxic injection to label these L6 SST interneurons. Scale bar: 100 μm. CC, corpus

408   callosum; HP, hippocampus.

409

Extended Data Fig. 5 Slide-seq data demonstrating changes in cortical interneurons in *Fezf2* mutants.

a, Representative Slide-seq data on a single coronal brain section of the SSp cortex from (left) a P37 WT mouse and (right) a P37 *Fezf2* KO mouse. **b,** Stacked Slide-seq data aligning multiple brain sections of P28-37 WT mice, illustrating the distribution of PNs. MO: n=4 ROIs, n=3 mice; SSp: n=8 ROIs, n=5 mice; VISp: n=4 ROIs, n=4 mice. **c,** Stacked Slide-seq data from 4-6 weeks old *Fezf2* KO mice. MO: n=3 ROIs, n=3 mice; SSp: n=6 ROIs, n=5 mice; VISp: n=4 ROIs, n=2 mice. **d-e,** Deep-layer PVALB and SST interneurons identified in control and *Fezf2* KO mutants (same dataset as in **b-c**), highlighting selective PVALB and SST interneuron subtypes. **f,** Ridge plots showing the distribution of selected PVALB and SST subtypes in control and *Fezf2* KO brains, demonstrating the shifted laminar location of PVALB-Fzd6 and SST-Chrna2 towards L6 in *Fezf2* mutants. The same dataset is used as in Fig. 2g.
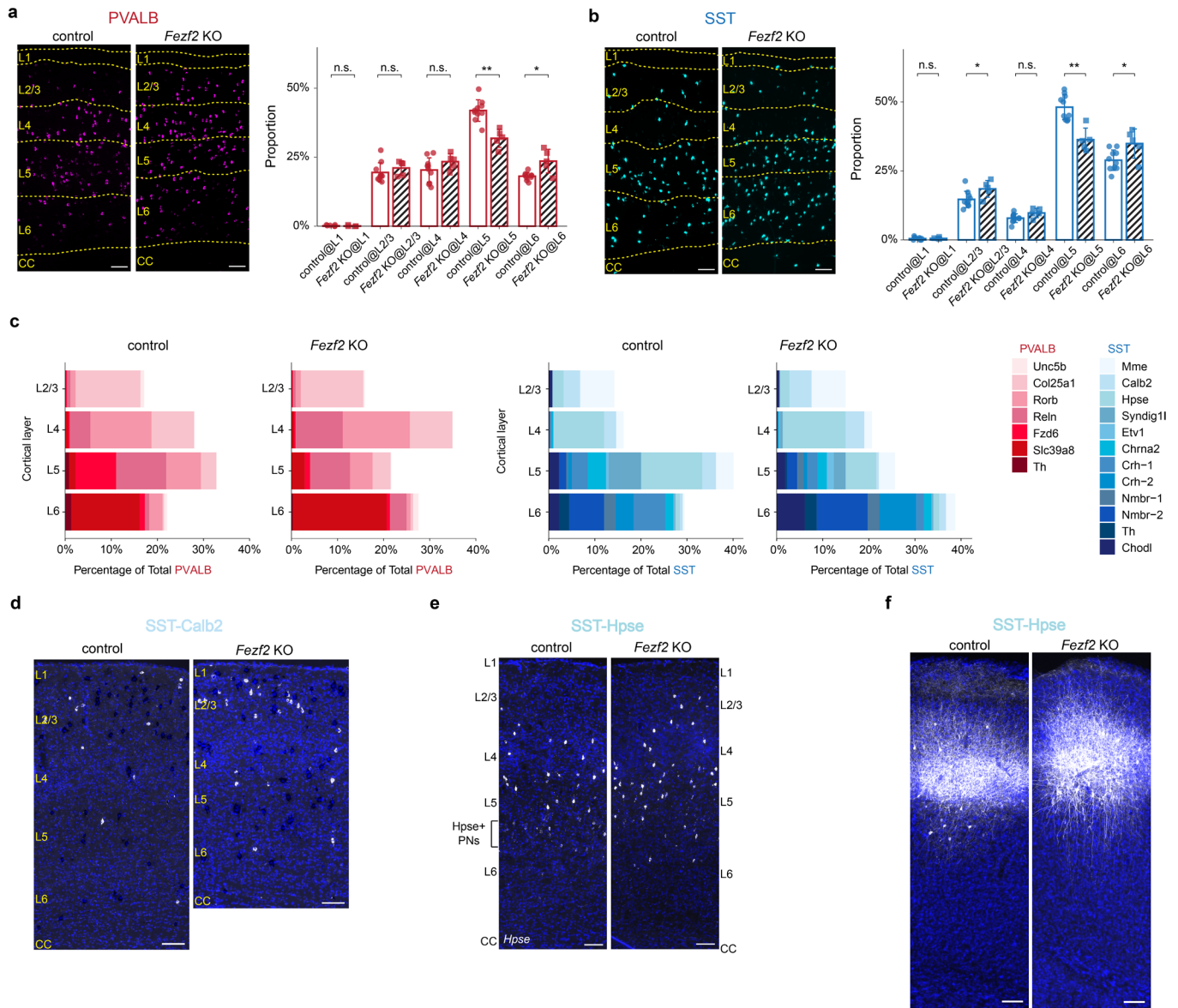
Extended Data Fig. 6 Shifted overall laminar distribution of PVALB and SST interneurons in *Fezf2* mutants.

a, (left) Representative RNAscope *in situ* hybridization images showing labeled *Pvalb* mRNA transcripts on fixed-frozen coronal sections of P28 control and *Fezf2* KO brains in the SSp region. Scale bar: 100 μm. (right) Bar plot illustrating the proportion of PVALB interneurons found in different cortical layers, compared between control and *Fezf2* KO brains. **b,** same as in **a**, based on RNAscope *in situ* hybridization against *Sst* mRNA. control: n=10 ROIs, n=5 mice (n=1 WT, n=2 *Bax* cHET, n=1 *Fezf2* HET_*Bax* cHET), age P26-28, n=3932 total PVALB interneurons, n=2280 total SST interneurons quantified. *Fezf2* KO: n=5 ROIs, n=2 mice (n=1 *Fezf2* KO, n=1 *Fezf2* KO_*Bax* cHET), n=2377 total PVALB interneurons, n=1677 SST interneurons quantified, age P27-28. Wilcoxon rank-sum test, n.s. not significant, p≥0.05; *p<0.05; **p< 0.01. Detailed p-values are provided in Supplemental Table 2. **c,** Bar plots showing the composition of each PVALB and SST interneuron subtypes in different cortical layers of control and *Fezf2* KO brains in the SSp region,

431   based on MERFISH dataset. control: n=3 ROIs, n=2 mice (n=1 WT, n=1 *Bax*_cHET), age: P14-30. *Fezf2* KO: n=3 ROIs,

432   n=3 mice (n=2 *Fezf2* KO, n=1 *Fezf2* KO_*Bax* cHET), age: P14-30. **d,** Representative RNAscope *in situ* hybridization

433   images showing SST-Calb2 interneurons, showing no obvious shift in the laminar distribution of these interneurons in

434   *Fezf2* KO mouse cortices in the SSp region. The signal was shown as the subtraction of *Vip* signal from *Calb2* signal.

435   Note that this strategy also labels SST-Chodl interneurons. **e,** Representative RNAscope *in situ* hybridization images

436   showing labeled *Hpse* mRNA transcripts on fixed-frozen coronal sections of P31 control and *Fezf2* KO brains in the SSp

437   region, demonstrating a laminar shift of SST-Hpse interneurons to more superficial layers. Note that L5 PNs express a

438   low level of *Hpse* gene. Scale bar: 100 µm. **f,** Representative images of labeled SST-Hpse interneurons in control and

439   *Fezf2* mutants at P47. AAV-PHP.eB-hDlx-DIO-ChR2-mCherry virus was introduced to the SSp of control

440   ($Hpse^{Cre}$;$Fezf2^{lacZ/+}$) and *Fezf2* mutant ($Hpse^{Cre}$;$Fezf2^{lacZ/lacZ}$) mice via stereotaxic injection to label these SST interneurons.

441   Scale bar: 100 µm.

442
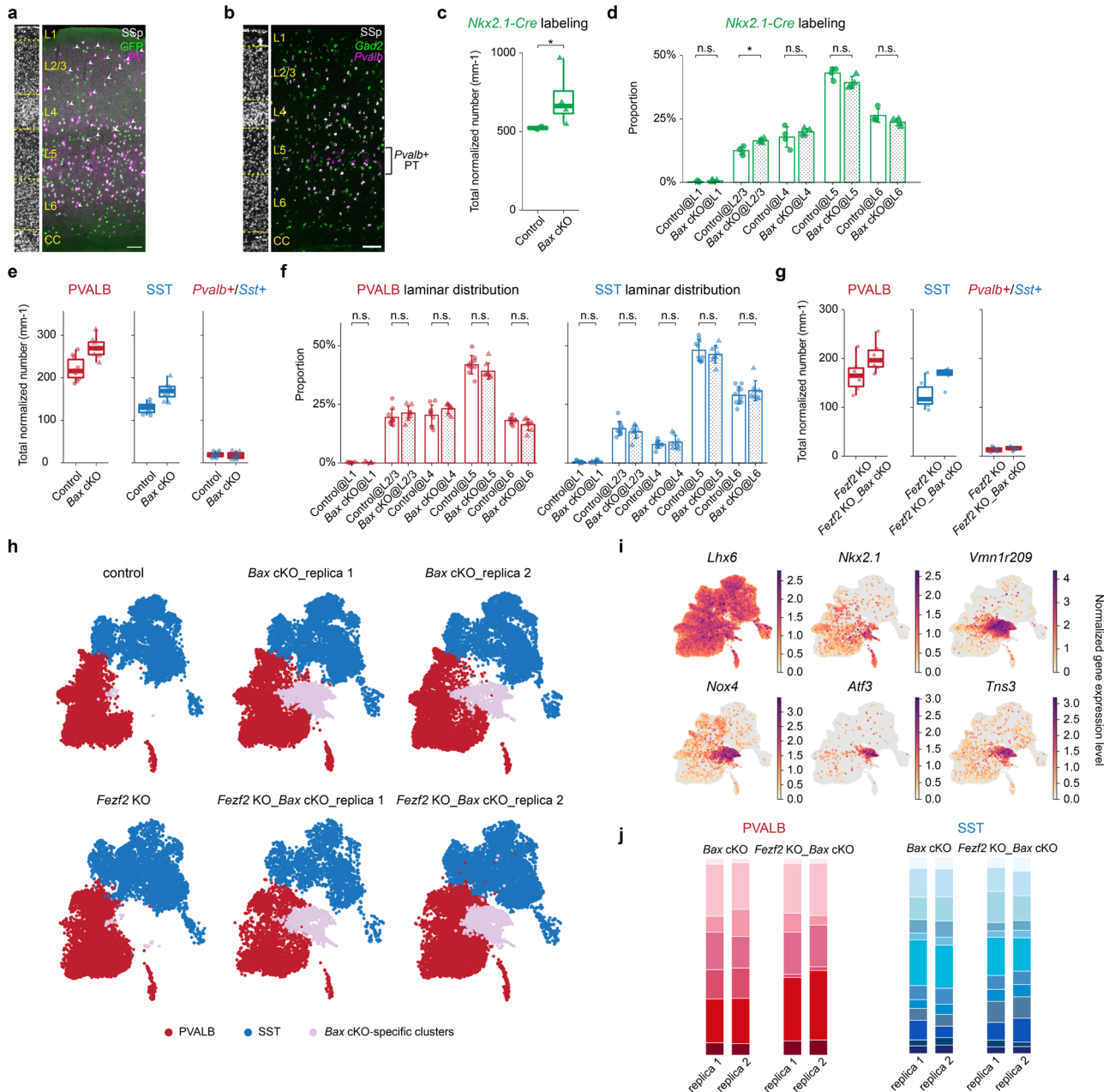
Extended Data Fig. 7 Conditional removal of *Bax* in PVALB and SST interneurons increases their number.

a, Representative image of coronal brain sections from a P26 *Nkx2.1-Cre;Bax$^{fl/+}$;Rosa26$^{LSL-h2b-GFP}$* mouse, immunostained

against GFP and PV, illustrating the incomplete labeling of superficial PV interneurons in the SSp region. Scale bar: 100

μm. **b,** Representative RNAscope *in situ* hybridization images showing labeled *Pvalb* and *Gad2* mRNA transcripts,

highlighting the expression of *Pvalb* gene outside of interneurons, specifically in *Gad2*- L5b PT neurons in the SSp

region. Scale bar: 100 μm. **c,** Quantification of genetically labeled interneurons by *Nkx2.1-Cre;Rosa26$^{LSL-h2b-GFP}$* in control

and *Bax* cKO conditions. control: n=3 mice (n=2 *Bax* cHET, n=2 *Fezf2* HET_*Bax* cHET), n=2316 GFP+ interneurons

counted; *Bax* cKO: n=4 mice (n=2 *Bax* cKO, n=2 *Fezf2* HET_*Bax* cKO), n=3548 GFP+ interneurons counted. **d,** Laminar

distribution of genetically labeled interneurons compared between control and *Bax* cKO conditions. Same dataset as in **c**.

453 Error bars show standard deviations. **e,** Quantification of PVALB and SST interneurons in control and *Bax* cKO cortices

454 in the SSp region, based on results from RNAscope *in situ* hybridization of fixed-frozen brain sections. L5 PT neurons

455 were identified as *Pvalb+/Lhx6-* cells located in L5b and subsequently excluded from the quantification. Numbers are

456 normalized to the length of the outskirts of the cortex in millimeters. control: n=10 ROIs, n=5 mice (n=1 WT, n=2 *Bax*

457 cHET, n=1 *Fezf2* HET_*Bax* cHET), age P26-28, n=3932 total PVALB interneurons, n=2280 total SST interneurons,

458 n=337 *Pvalb+/Sst+* interneurons. *Bax* cKO: n=8 ROIs, n=4 mice (n=2 *Bax* cKO, n=2 *Fezf2* HET_*Bax* cKO), age P26-28,

459 n=3470 total PVALB interneurons, n=2150 total SST interneurons, n=221 total *Pvalb+/Sst+* interneurons quantified. **f,**

460 Same dataset as in **d**, showing the distribution of PVALB and SST interneurons in different cortical layers was not altered

461 in *Bax* cKO. Error bars show standard deviations. **g.** Quantification of PVALB and SST interneurons in *Fezf2* KO and

462 *Fezf2* KO_*Bax* cKO cortices, based on RNAscope *in situ* hybridization of fresh-frozen sections. *Fezf2* KO: n=6 ROIs, n=4

463 mice (n=1 *Fezf2* KO, n=3 *Fezf2* KO_*Bax* cHET), age P28-33, n=1668 total PVALB interneurons, n=1257 total SST

464 interneurons, n=138 total *Pvalb+/Sst+* interneurons quantified. *Fezf2* KO_*Bax* cKO: n=6 ROIs, n=4 mice, age P28-33,

465 n=2161 total PVALB interneurons, n=1768 total SST interneurons, n=175 total *Pvalb+/Sst+* interneurons quantified. **h,**

466 UMAP plots of P14 snRNA-seq data on interneurons from four different genotypes, showing a group of cells that are

467 specific to the *Bax* cKO and *Fezf2* KO_*Bax* cKO conditions. **i,** UMAP plots showing the normalized gene expression

468 level of selected genes that are expressed in *Bax* cKO-specific clusters. **j,** Stacked bar plots showing that the proportion of

469 different PVALB and SST interneurons remains relatively consistent across biological replicates of snRNA-seq of cortical

470 interneurons from *Bax* cKO and *Fezf2* KO_*Bax* cKO brains. **d** and **f,** Wilcoxon rank-sum test, n.s. not significant, p≥

471 0.05; *p<0.05. Detailed p-values are provided in Supplemental Table 2.

472

473

474
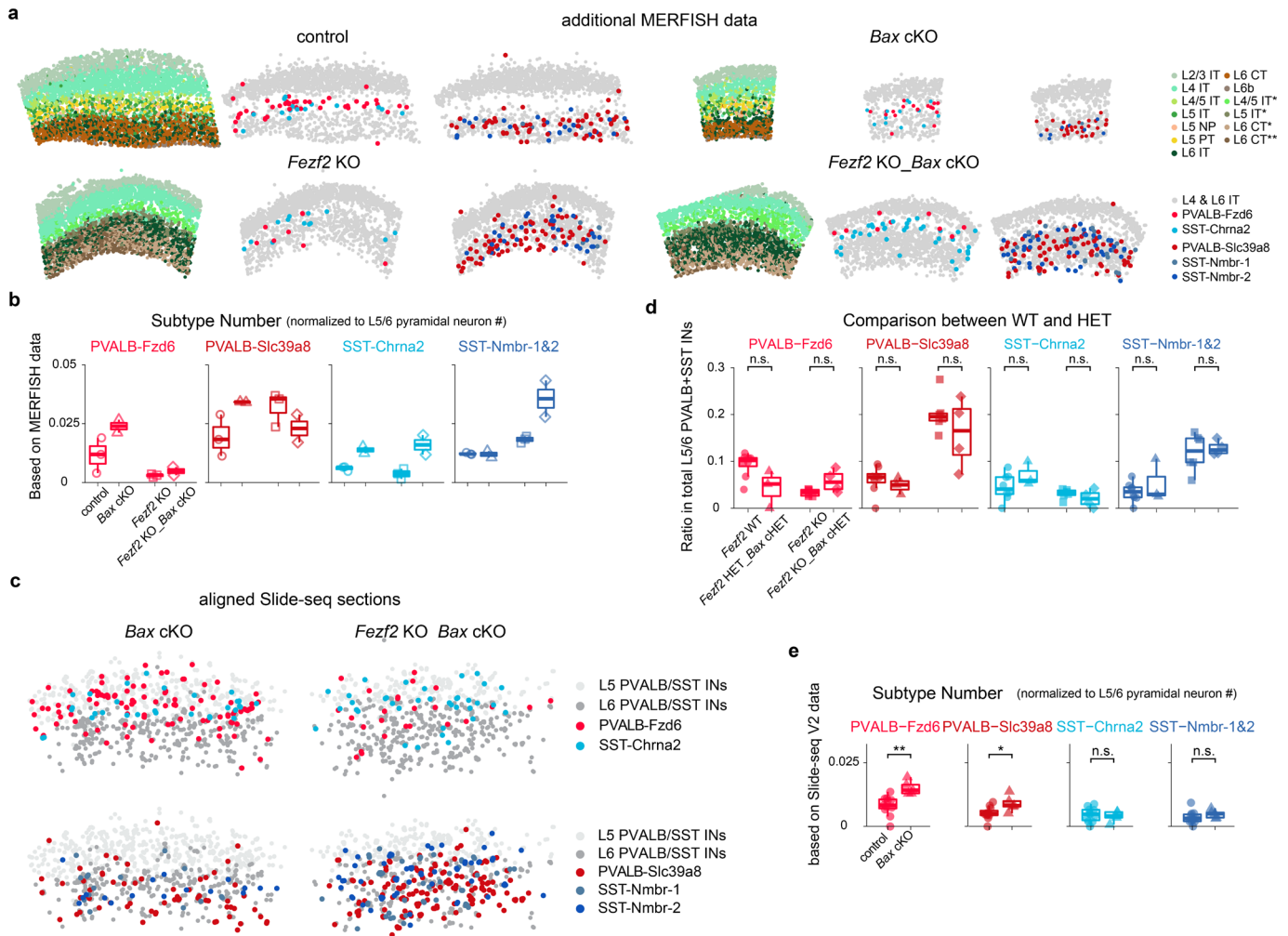
Extended Data Fig. 8 Spatial transcriptomics data showing the effects of selective removal of *Bax* in PVALB and SST interneurons on the interneuron phenotypes of *Fezf2* mutants.

a, Additional P14 MERFISH data of different genotypes not included in Fig 3d. **b,** Number of selected PVALB and SST subtypes normalized to the number of L5/6 PNs in four different genotypes based on MERFISH data in the SSp region. No statistical test was applied due to the small dataset size. **c,** Aligned and stacked Slide-seq data on coronal brain sections from *Bax* cKO and *Fezf2* KO_*Bax* cKO mice, highlighting selected PVALB and SST interneuron subtypes identified in L5/6. *Bax* cKO: n=5 ROIs, n=3 mice; *Fezf2* KO_*Bax* cKO: n=4, n=3 mice. Age range: P28-33. **d,** Ratio of selected PVALB and SST interneuron subtypes within total L5/6 PVALB and SST interneurons are consistent between wildtype and heterozygous genotype in the SSp region, based on Slide-seq data. *Fezf2* WT: n=8 ROIs, n=5 mice; *Fezf2* HET_*Bax* cHET: n=3 ROIs, n=2 mice; *Fezf2* KO: n=6 ROIs, n=5 mice; *Fezf2* KO_*Bax* cHET: n=4 ROIs, n=2 mice. Age range: 4-6 weeks old. These data are included in Fig. 2g. **e,** Number of selected PVALB and SST subtypes normalized to the number of L5/6 PNs compared between control and *Bax* cKO. Control: n=11 ROIs, n=7 mice; *Bax* cKO: n=5 mice. Age range: P28-37. For **b** and **e**, Wilcoxon rank-sum test. n.s. not significant, $p \geq 0.05$; *$p<0.05$; **$p< 0.01$; ***$p<0.001$. Detailed p-values are provided in Supplemental Table 2.

489
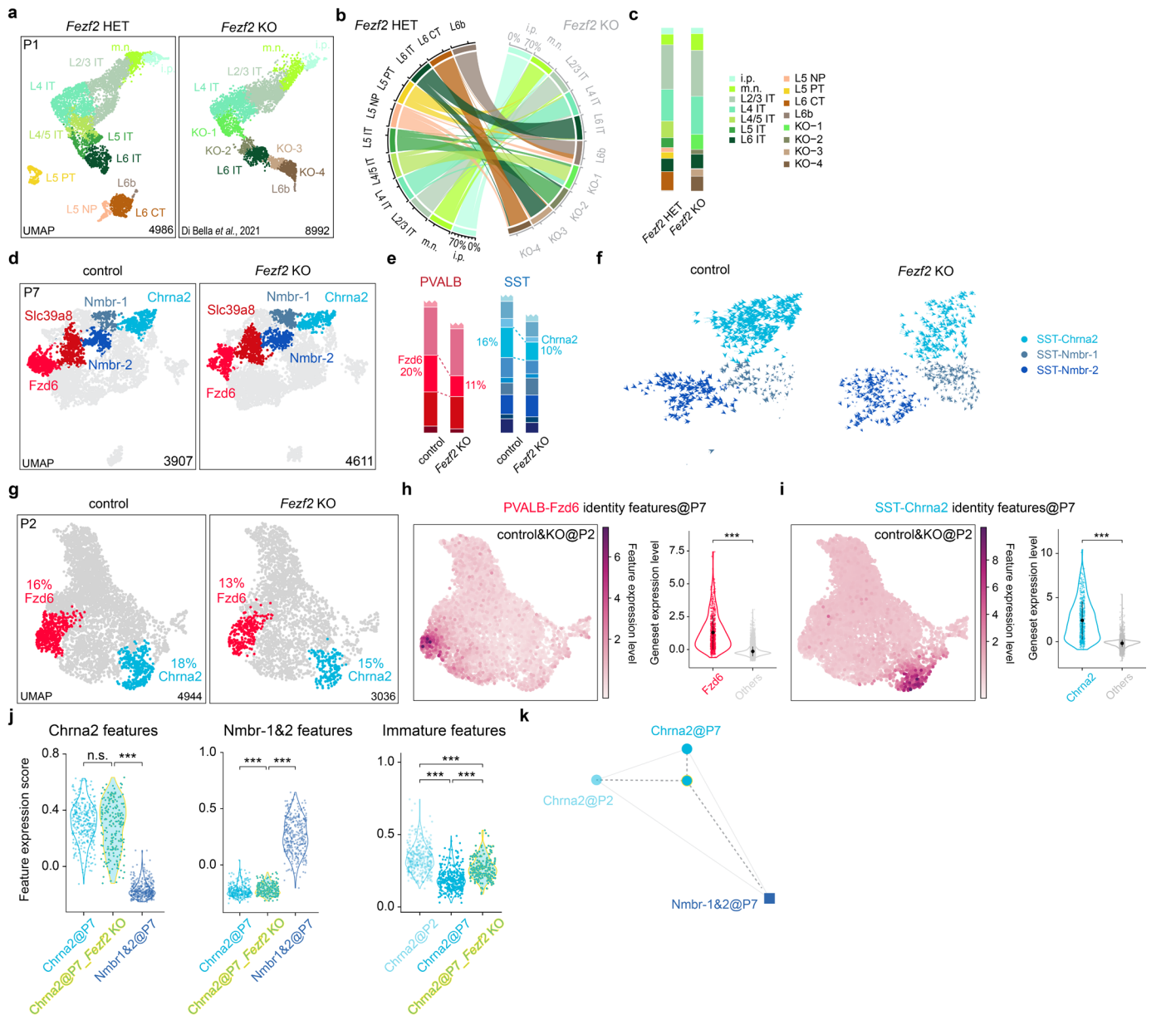
Extended Data Fig. 9 Changes in interneurons in *Fezf2* mutant at early developmental ages

a, UMAP visualization of published snRNA-seq data[41] of excitatory neurons from P1 *Fezf2* HET and *Fezf2* KO mouse

cortices. **b,** River plot illustrating the correspondence of each PN type between P1 *Fezf2* HET and *Fezf2* KO conditions

based on transcriptomic similarity, showing the proportion of mapped PN cell types within each cell type in *Fezf2* KO. **c,**

Stacked bar plots showing the composition of excitatory neuron types in *Fezf2* HET and *Fezf2 KO* brains based on

snRNA-seq data. **d,** UMAP visualization of snRNA-seq data of cortical interneurons collected from control (*Dlx5/6-

Cre;Fezf2^{lacZ/+};Rosa26^{LSL-h2b-GFP}*) and *Fezf2* KO (*Dlx5/6-Cre;Fezf2^{lacZ/lacZ};Rosa26^{LSL-h2b-GFP}*) mouse brains at P7, with

selected PVALB and SST interneuron subtype highlighted. **e,** Stacked bar plots showing the proportion of deep-layer

PVALB and SST subtypes in control and *Fezf2* KO brains based on snRNA-seq data. **f,** RNA velocity analysis of snRNA-

seq data on cortical interneurons collected from control (*Fezf2* HET) and *Fezf2* KO mouse brains at P7, showing gene

500 expression dynamics of three SST interneuron subtypes. **g,** UMAP visualization of snRNA-seq data of cortical

501 interneurons collected from control (*Nkx2.1-Cre;Fezf2$^{lacZ/+}$;Bax$^{fl/+}$;Rosa26$^{LSL-h2b-GFP}$*) and *Fezf2* KO (*Nkx2.1-*

502 *Cre;Fezf2$^{lacZ/lacZ}$;Bax$^{fl/+}$;Rosa26$^{LSL-h2b-GFP}$*) mouse brains at P2, with PVALB-Fzd6 and SST-Chrna2 interneuron subtypes

503 highlighted. **h-i,** Feature genes identified in the P7 snRNA-seq dataset that are selectively expressed in PVALB-Fzd6 and

504 SST-Chrna2 interneuron subtypes are also selectively expressed at P2. (left) UMAP plot showing the expression level of

505 feature genes. (right) Violin plot comparing the expression level of feature genes in a particular cluster versus the rest of

506 the nuclei. **j,** The expression score of gene sets characteristic of SST-Chrna2, SST-Nmbr-1&2 at P7, and SST-Chrna2 at

507 P2 (referred to as Chrna2 feature, Nmbr-1&2 feature, and immature features, respectively; see Methods) were compared

508 between different groups of SST interneurons. **k,** Triangular Affinity Map of SST-Chrna2 interneurons in *Fezf2* mutants

509 at P7 (see Methods), showing the relative transcriptomic similarities among SST-Chrna2 at P7, SST-Nmbr-1&2 at P7, and

510 SST-Chrna2 at P2.
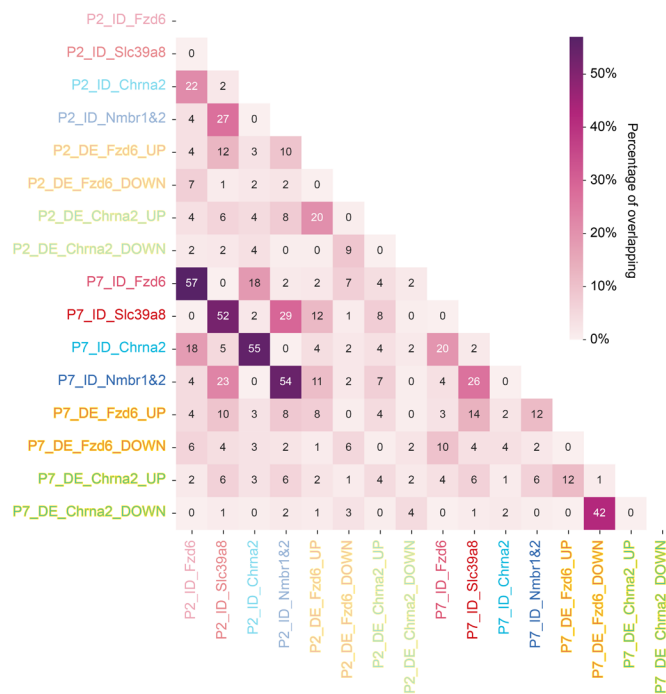
Extended Data Fig. 10 Heatmap showing the percentage of overlap between different gene sets.

Methods

Mice

All experimental procedures were approved by the Harvard Medical School Institutional Care and Use Committee and were performed in compliance with the Guide for Animal Care and Use of Laboratory Animals. Mice were housed in a temperature-controlled and humidity-controlled facility and were maintained on a 12–12 h dark-light cycle. All experiments were performed on animals of both sexes. Whenever possible, mice of both sexes are used in experiments. Experiments were not blinded because mice and treatments were easily identifiable as experiments were performed. Sample sizes were not predetermined.

Mouse lines were used in this study include *Fezf2* KO (Ref [42]), *Rorb^Cre* mice (JAX #023536), *Tcerg1l^CreER* mice (JAX #034000), *Pvalb^FlpO* (JAX #022730), *Rosa26^FSF-LSL-tdTomato* (*Ai65*) (JAX #021875), *Dlx5/6-Cre* (JAX #008199), *Sst^Cre* (JAX #018973), *Sst^FlpO* (JAX #031629), *Chrna2-Cre* (Ref [19]), *Pdyn^Cre* (JAX #027958), *Npy^FlpO* (JAX #030211), *Rosa26^LSL-tdTomato* (*Ai14*) (JAX #007914), *Crhr2^Cre* (JAX #033728), *Hpse^Cre* (JAX #037334), *Nkx2.1-Cre* (JAX #008661), *Bax^fl* (MGI ID:3589203), *Rosa26^LSL-h2b-GFP* (JAX #036761).

snRNA-seq

Nuclei suspension preparation and library construction. Brain samples were harvested from mice with specific genotypes and ages, and the cortex was carefully dissected in ice-cold Homogenization Buffer (HB) comprising 0.25 M sucrose, 25 mM KCl, 5 mM MgCl$_2$, 20 mM Tricine-KOH, 1 mM DTT, 0.15 mM spermine, and 0.5 mM spermidine. The dissected brain tissue was then transferred to a 2 ml Dounce tissue grinder filled with HB supplemented with 0.15-0.25% IGEPAL-CA630 and 0.2 U/µl RNasin. Tissue homogenization was performed with 8-10 strokes of pestle A followed by 9-10 strokes of pestle B. The homogenate was filtered through a 30 µm filter into a 15 ml conical tube and centrifuged at 500 g for 5 min. at 4 °C using a swinging-bucket centrifuge. The resulting pellet was resuspended in 1X PBS containing 1% BSA + 0.2 U/µl RNasin and then passed through a 40 µm filter. DRAQ5 (BioLegend) was added to the nuclei suspension for sorting of GFP+ nuclei on a Sony MA900 cell sorter using a 70 µm nozzle (see Supplemental Methods). Nuclei were collected in a pre-chilled 0.2 ml PCR tube and counted using a hemocytometer (INCYTO C-Chip). snRNA-seq libraries were prepared using the Chromium Single Cell 3' Kit v3.1 (10x Genomics), following the manufacturer's protocol. Pooled libraries were sequenced on NovaSeq 6000 instruments (Illumina).

543 **snRNA-seq data processing.** CellRanger (v7.0.0, 10x Genomics) was used with default parameters to map snRNA-seq

544 data to the mouse reference genome (mm10) provided by 10x Genomics. The gene expression matrices output from

545 CellRanger were then imported into Python v3.9.13 as AnnData objects (anndata v0.8.0). Scanpy v1.9.1 was used as the

546 basic framework for snRNAseq processing. We used Scrublet v.0.2.3[43] to calculate the potential doublet score for each cell.

547 Unless specified elsewhere, genes expressed in fewer than 3 cells were filtered. Cells were filtered based on the following

548 criteria: n_counts < 15,000, 200 < n_genes < 4,000, ratio_of_mitochondria_genes < 5% (gene symbols beginning with 'mt-

549 '), ratio_of_ribosome_genes < 5% (gene symbols beginning with 'Rpl' or 'Rps') and scrublet_score<0.25. After quality

550 control, the raw counts were normalized using the pp.normalize_total function (counts_per_cell_after = 10,000); the

551 normalized counts were log-transformed using the pp.log1p function. The Pearson residuals were calculated from the raw

552 counts for selecting the top 5,000 highly variable genes using experimental.pp.highly_variable_genes function

553 (n_top_genes=5,000). The StandardScaler function (with_mean=False) of scikit-learn v.0.24.0 was then used to scale the

554 Pearson residuals of highly variable genes, followed by the TruncatedSVD function of scikit-learn v.0.24.0 to calculate the

555 Principal Component Analysis (PCA) embeddings for the cells. The unsupervised graph-based Leiden clustering algorithm,

556 pp.neighbors and tl.leiden functions, was used for the clustering based on the PCA embeddings. To sub-cluster specific

557 clusters, the piaso.tl.leiden_local function from our single-cell analysis toolkit PIASO (https://github.com/genecell/PIASO)

558 was used. This function repeats the steps of highly variable gene selection, PCA embedding and Leiden clustering on

559 selected cells while maintaining the clustering results for the remaining cells. After clustering, COSG[44] was used to identify

560 top marker genes for each cluster, which were cross-compared with well-known marker genes from literature for cell type

561 annotation. For visualization of multiple snRNA-seq datasets across different conditions, we employed the

562 piaso.pl.plot_embeddings_split from PIASO to align cell coordinates from different conditions and scale the gene

563 expression or cell metrics for consistency.

564 **Source and processing of public scRNA-seq datasets.** The P28 mouse cortex interneuron snRNA-seq dataset (GEO

565 accession number: GSE164570)[17], P14 control and *Fezf2* KO mouse S1 cortex snRNA-seq datasets (GEO accession number:

566 GSE158096)[30], and P1 *Fezf2* Het and *Fezf2* KO mouse cortex scRNA-seq datasets (GEO accession number: GSE153164)[41]

567 were downloaded and processed by re-mapping the FASTQ files using CellRanger (v7.0.0, 10x Genomics) with default

568 parameters as described above. The processed and annotated SMART-Seq V4 scRNA-seq datasets were downloaded from

569 previous publications[18,45] and re-annotated.

570   **Individual cell-based differential transcriptomic analysis across conditions.** To assess transcriptomic differences across

571   different conditions, we developed a novel algorithm named Emergene. This method performs independent of cell clustering,

572   and hence overcomes the biases associated with existing differentially expressed gene (DEG) analysis methods, which can

573   be skewed by cluster size. First, Emergene identifies genes with localized expression patterns by generating two gene

574   expression diffusion maps. One map diffuses gene expression locally to k-nearest neighbors (kNN), while the other diffuses

575   gene expression randomly to k number of cells. The deviation of these two diffusion maps from the original gene expression

576   map is measured by cosine similarity, a technique employed in COSG. Genes showing specific expression patterns are

577   identified based on the differences between the deviations of the two diffusion maps from the original map. Next, Emergene

578   uses a similar strategy to identify genes with differential expression patterns across conditions. It compares and contrasts

579   the diffusion gene expression pattern to k-nearest neighbor on shared cell embeddings across conditions. Together,

580   Emergene identifies a combinatorial gene set that includes genes exhibiting distinctive expression patterns among local cell

581   neighbors under different conditions. Based on the expression level of these genes, Emergene incorporated the permutation

582   test, as used in scDRS for the GWAS risk genes enrichment analysis with improved computational efficiency and scalability,

583   to identify cells with enriched expression of genes that showed specific expression patterns within and across conditions.

584   To determine statistical significance for each individual cell, Emergene generated 10,000 sets of Monte Carlo samples of

585   control gene sets with matched gene set size, expression mean, and expression variance. The P values of individual cells

586   were then computed based on the empirical distribution of the normalized expression scores across all cells and all control

587   gene sets. Finally, P value for each cell type can be assigned through a gliding threshold (50th percentile by default) based

588   on P values of individual cells within each cluster.

589   **Feature gene set identification and calculation of expression score.** The identity (ID) feature gene list of a specific

590   interneuron subtype was comprised of the top 200 marker genes identified by COSG that were differentially expressed

591   between the two PVALB or SST subtypes. The immature feature genes were the top 200 differentially expressed (DE) genes

592   identified by COSG that expressed higher at P2 than at P7 for specific interneuron subtypes. DE genes between control and

593   *Fezf2* KO conditions were the top 200 DE genes identified by COSG across conditions for specific interneuron subtypes.

594   The tl.score_genes function from Scanpy v1.9.1 was used to compute the enrichment score of feature gene expression for

595   each individual cell.

596   **Triangular Affinity Map for comparative visualization of gene expression similarity**. To generate a visual

597   representation of transcriptomic similarity between one target cell type and three anchor cell types, we employed the

598 Triangular Affinity Map (TAMap) based on gene set expression scores. We first applied min-max normalization to adjust

599 the mean gene set expression scores across various cell type comparisons to a uniform scale, ensuring consistency in the

600 similarity metrics. We subsequently calculated the sizes of three internal angles, each spanned by the target cell type and

601 one of the anchor cell types. These angles represent the similarities between two anchor cell types—such that their sum

602 equaled 360 degrees. Additionally, we computed the edge lengths connecting the target cell type with each anchor cell type

603 based on the similarities between the target cell type and each anchor cell type. For a 2D visualization in a Cartesian

604 coordinate system, the target cell type was positioned at the origin, and one anchor cell type along the positive y-axis.

605 Matplotlib v3.5.2 was utilized to generate the final visual representation.

606 **RNA velocity**. To predict how the gene expression pattern of each cell type will change developmentally, we employed

607 scVelo v0.2.4[35] to infer the RNA velocity from the ratio of spliced and unspliced reads. STAR 2.7.10a was used to quantify

608 the counts of spliced and unspliced reads in individual cells from the P7 *Fezf2* HET and P7 *Fezf2* KO snRNA-seq FASTQ

609 files. Next, we mapped the information of annotated cell types and UMAP coordinates based on cell barcodes. RNA

610 velocities were computed using the scvelo.tl.recover_dynamics, scvelo.tl.velocity(mode='dynamical') and

611 scvelo.tl.velocity_graph() functions, and visualized based on UMAP coordinates with the scvelo.pl.velocity_embedding()

612 function.

613

614 **MERFISH**

615 **Selection of probe set.** To design the MERFISH gene panel that captures the transcriptomic heterogeneity across cell types,

616 developmental stages, and genotypes, we utilized multiple snRNA-seq datasets collected across a wide age range. Top

617 marker genes identified by COSG were combined with known marker genes from literature to generate an initial gene panel

618 for late postnatal ages. Additional genes were added and tested on scRNA-seq collected from younger ages to ensure

619 comprehensive cell type identification across ages. RNA targets were selected based on maximizing unique probe sites per

620 gene for high detection rate while minimizing combinatorial optical crowding for MERFISH imaging. A fluorescently

621 labeled oligonucleotide library probing for 293 combinatorial genes and 4 sequential genes, including GFP was selected.

622 The resulting readout and encoding probes were manufactured by Vizgen Inc. The full list of probes is available in

623 Supplemental Table 1.

624 **MERFISH sample processing.** Whole intact brain samples were collected in RNase-sterile conditions, flash-frozen in

625 liquid nitrogen, and moved to 5 mL Eppendorf tubes, and stored at −80 °C for tissue microarray (TMA) construction and

626   MERFISH. First, frozen cortical tissues were collected using 2 mm or 3 mm disposable biopsy punch needles from specific

627   brain regions. The tissue punches were then trimmed uniformly with a sterile razor blade, oriented laterally, and embedded

628   within a pre-formed scaffold of Optimal Cutting Temperature media. On average, six sample punches were assembled into

629   each TMA. All samples were prepared in RNase-sterile conditions for MERFISH imaging according to the procedure

630   described in a previous publication[46] and using select additional kits and instruments offered through Vizgen Inc. Briefly,

631   the TMA samples were cryosectioned at 10 μm using a cryostat (Leica) at -20°C, and mounted and melted onto fluorescent

632   microsphere-coated, functionalized coverslips, fixed with 4% PFA in 1X PBS, and permeabilized overnight in 70% ethanol.

633   TMA sections were stained using the Cell Boundary Stain Kit (Vizgen, PN 10400009). Following a 1-hour room

634   temperature blocking step in Cell Boundary Block Buffer containing 40 U/μl murine RNase inhibitor, samples were

635   incubated in the primary and secondary antibody cocktails for 1 hour each, with interspersed 1X PBS washes. Primary

636   antibodies against specific proprietary cell membrane proteins and oligo-conjugated secondary antibodies were diluted in

637   Cell Boundary Block Buffer containing 40 U/μl murine RNase inhibitor, with dilution factors of 1:100 and 3:100,

638   respectively. Antibody labeling was fixed again with 4% PFA for 15 minutes. TMA sections were then hybridized with 70

639   μL of 297-gene probe library solution for 36-48 hrs in a humidified 37 °C incubator with a 2x2 cm square of Parafilm

640   layered onto the surface to prevent evaporation. Samples were embedded in a polyacrylamide gel by incubating the samples

641   in freshly prepared polyacrylamide gel solution (40% 19:1 acrylamide/bis-acrylamide solution, 5M NaCl, 1M Tris pH=8,

642   and nuclease-free water in a dilution of 1:3:3:39; gel solution combined with catalysts, 10% w/v ammonium persulfate

643   solution and NNN'Tetramethyl-ethylindiamin in a dilution of 2000:10:1). To achieve this, the coverslip containing TMA

644   samples were inverted onto the polyacrylamide solution aliquoted on the surface of a Gel-Slick treated, 2x3 inch microslide.

645   Non-targeted molecules were cleared from the gel-embedded sample within a detergent mixture (20X saline-sodium citrate,

646   10% sodium dodecyl sulfate solution, 25% Triton-X 100 solution, and nuclease-free water in a 5:10:1:34 ratio)

647   supplemented with 0.8 U/μl Proteinase K (NEB P8107S) for 48-72 hours in a humidified 37 °C incubator.

648   **MERFISH imaging and post-imaging processing.** Samples were further stained with DAPI and PolyT Staining Reagent

649   (Vizgen, PN 20300021), and imaged using MERSCOPE (Vizgen) with MERSCOPE 300-Gene Imaging Cartridges

650   (Vizgen, PN 20300017). Illumination intensities and exposure times were kept the same in every dataset, capturing images

651   of the whole TMA with both a 10× NA 0.25 and 60× NA 1.4 objective, at 7 z-positions per x–y location, separated by

652   1.5 μm. MERSCOPE post-imaging analysis used MERlin[47] to decode positions and copy numbers of target RNA species

653   into count matrices, and Cellpose[48] to generate cell boundary masks (software version 233.230615.567, segmentation

654   parameter: cell boundary 1).

655   **Cell type identification for MERFISH data.** After quality control, four major types of cells were identified based on

656   marker gene expression into excitatory neurons, two groups of interneurons (one group consisting of PVALB and SST, and

657   another consisting of VIP, LAMP5, and SNCG interneurons) and non-neuronal cells. Each group was separately annotated

658   using the marker Gene-guided Dimensionality Reduction (GDR) algorithm developed by our team. GDR integrates

659   annotated snRNA-seq data and unannotated MERFISH data, by first applying unsupervised Leiden clustering to MERFISH

660   data, followed by identification of the top 15 marker genes for both the MERFISH clusters and the annotated snRNA-seq

661   cell types using COSG[44]. GDR calculates expression scores for these marker gene sets across both data modalities,

662   projecting cells into a shared low-dimensional gene expression space that reflects biological identity in each dimension. In

663   this space, cells with similar identities or gene expression patterns are located closely together. To further address technical

664   effects from different modalities, we used the pp.harmony_integrate function from Scanpy v1.9.1 with default parameters

665   to run the Harmony[49] integration procedure. Following this, Support Vector Machine (SVM) with the radial basis function

666   kernel was used to predict the cell types of cells in the MERFISH data based on the cell embeddings from both MERFISH

667   and snRNA-seq data. SVM was implemented through the svm.SVC function from scikit-learn v.0.24.0, set to kernel=`rbf`,

668   and   class_weight=`balanced`.   The   GDR   code   is   available   in   the   PIASO   GitHub   repository

669   (https://github.com/genecell/PIASO), and implemented via the piaso.tl.predictCellTypeByGDR function.

670   **Analysis of Allen MERFISH data.** The MERISH spatial transcriptomics data of a single adult mouse brain (Allen

671   MERFISH data) with a 500 gene panel was published in Yao *et al.*, 2023[18]. The processed and spatially aligned data with

672   raw   counts   was   downloaded   from   Allen   Brain   Cell   Atlas   (C57BL6J-638850-raw.h5ad;

673   https://alleninstitute.github.io/abc_atlas_access/descriptions/MERFISH-C57BL6J-638850.html). We subset the MOp,

674   MOs, SSp and VISp regions based on the "parcellation_structure" annotation as the data was registered to the Allen CCFv3

675   (Common Coordinate Framework). The dataset was also further divided into four major cell type groups and annotated

676   separately using snRNA-seq or scRNA-seq reference with GDR as described above. Specifically, 10x Genomics v3 snRNA-

677   seq datasets was used as reference for interneurons. SMART-Seq v4 scRNA-seq datasets were used as references for

678   excitatory neuron and non-neuronal cells. QC and cell type annotation of these reference datasets were performed as

679   described above.

680

681 **Slide-seq**

682 **Library generation and sequencing.** Slide-seq pucks (round, 3 mm in diameter) were generated as described previously[50].

683 10 µm-thick coronal sections were obtained from flash-frozen brain samples using cryostat (Leica) and used for generating

684 Slide-seq library immediately, following published Slide-seqV2 protocol[40,51]. Libraries were pooled and sequenced on

685 NovaSeq 6000 flow cells (Illumina). One published Slide-seq data on mouse cortex SSp region was included in this study,

686 puck 200306_02, can be downloaded at https://singlecell.broadinstitute.org/single_cell/study/SCP815/highly-sensitive-

687 spatial-transcriptomics-at-near-cellular-resolution-with-slide-seqv2.

688 **Slide-seq data pre-processing.** The sequenced reads were aligned to GRCm39.103 reference and processed using the Slide-

689 seq tools pipeline (https://github.com/MacoskoLab/slideseq-tools; v.0.2) to generate the gene count matrix and match the

690 bead barcode between array and sequenced reads. The spatial barcode recovery step was further optimized with customized

691 algorithm.

692 **Cell type mapping using RCTD.** We used RCTD[52] (now available in the R package spacexr v2.2.1) to map cell types in

693 Slide-seq data based on reference scRNA-seq data. The reference dataset was processed by first retaining only the genes

694 detected in both the Slide-seq data and the reference scRNA-seq data. We then used the R version of COSG (v0.9.0) with

695 the following parameters: mu=100, remove_lowly_expressed=TRUE, expressed_pct=0.1, to select the union set of the top

696 100 marker genes for each cell type in the annotated scRNA-seq reference. This processed scRNA-seq dataset was then

697 used as input for RCTD. The extraction of distinctive features for each cell type in the reference dataset increased the

698 accuracy of cell type decomposition in Slide-seq data. From the RCTD output, we retained beads classified as `singlet` or

699 `doublet_certain` and excluded the rest.

700 **Inference of interneuron laminar locations in MERFISH and Slide-seq data.** The resident cortical layer for each

701 interneuron was assigned based on the identity of its five nearest excitatory neuron neighbors. Specifically, the KDTree

702 function from scikit-learn v.0.24.0 with leaf_size=6 and k=5 was used for this purpose.

703

704 **RNAscope *in situ* hybridization**

705 For fixed-frozen brain tissue, mice were deeply anesthetized with sodium pentobarbital (Euthasol) via intraperitoneal

706 injection and transcardially perfused with 1X PBS followed by 4% paraformaldehyde (PFA). Brains were then dissected

707 and post-fixed in 4% PFA overnight at 4°C. PFA-fixed brain samples were cryopreserved in 30% (w/v) sucrose and

708 sectioned into 20 µm coronal slices using a sliding microtome (Leica). Brain slices were preserved in the Storage Buffer,

709 comprising 28% (w/v) sucrose, 30% (v/v) ethylene glycol in 0.1 M sodium phosphate buffer, at -80 °C until further

710 processing. For fresh-frozen brain tissue, flash-frozen brain samples were sectioned on a cryostat (Leica) into 19-20 μm

711 coronal slices. mRNA transcripts were detected using the RNAscope Multiplex Fluorescent V2 Assay Kit (ACDBio,

712 323100), following manufacturer's protocol for either tissue type with the following modification. Tissue was digested

713 using Protease III for 30 min. at room temperature. The RNAscope catalogue probes used included *Lhx6* (#422791), *Gad2*

714 (#439371), *Sst* (#404631), *Pvalb* (#421931), *Crhr2* (#413201), *Nmbr* (#406461), *Calb2* (#313641), *Hpse* (#412251).

715

716 **Image acquisition**

717 Images of RNAscope *in situ* hybridization experiments were collected using a tiling scope (Zeiss Axio Imager A1) with a

718 10X objective. Images of transgenic mouse line labeling were either collected using a whole slide scanning microscope with

719 a 10X objective (Olympus VS120 slide scanners), or acquired with an upright confocal microscope (Zeiss LSM 800) with

720 a 10X objective (Plan-Apochromat 10x/0.45 M27) or a 20X objective (Plan-Apochromat 20x/0.8 M27) to better appreciate

721 the cellular morphology. Images of viral genetic labeling of SST-Hpse and SST-Crhr2 were imaged using another confocal

722 microscope (Leica Stellaris) with a 10X objective (HC PL APO 10x/0.40 DRY). Stitching of image tiles was mostly

723 performed using acquisition software, except for some used Stitching plugin in FiJi[53].

724

725 **Statistics**

726 Most of the statistical tests in this study employed two-sided non-parametric tests due to the small sample sizes (n<25) and

727 the non-normal distribution of single-cell expression data. Boxplots display the median, the 25th percentile, the 75th

728 percentile, with two whiskers that extend to 1.5 times the interquartile range. A summary of statistical test results is provided

729 in Supplementary Table 2.

730

731

732 **Data availability**

733 The data have been deposited at the Gene Expression Omnibus (GEO) under accession number GSE272706, and at the

734 Single Cell Portal: https://singlecell.broadinstitute.org/single_cell/study/SCP2716/pyramidal-neurons-control-the-number-

735 and-distribution-of-cortical-interneuron-subtypes.

736

Code availability

Emergene is available via https://github.com/genecell/Emergene, and PIASO is available via https://github.com/genecell/PIASO.

Author Contributions

S.J.W. and G.F. designed the study. S.J.W., S.Y., C.M., Y.Q. performed experiments. M.D., S.J.W. performed data analysis. G.J.M., E.Z.M., F.C. provided materials and expertise for Slide-seq experiments. S.L.F. provided access to MERFISH expertise. Q.X. constructed the viral plasmid. J.A.S. and D.J.D. provided samples from mouse models. S.J.W., M.D., C.M., G.F. wrote the manuscript with feedback from S.L.F.

Competing interests

Gord Fishell is a founder of Regel Therapeutics, which has no competing interests with the present manuscript.

References

1. Tasic, B. *et al.* Adult mouse cortical cell taxonomy revealed by single cell transcriptomics. *Nat Neurosci* **19**, 335–346 (2016).

2. Yao, Z. *et al.* A taxonomy of transcriptomic cell types across the isocortex and hippocampal formation. *Cell* **184**, 3222-3241.e26 (2021).

3. Tasic, B. *et al.* Shared and distinct transcriptomic cell types across neocortical areas. *Nature* **563**, 72–78 (2018).

4. Wu, S. J. *et al.* Cortical somatostatin interneuron subtypes form cell-type-specific circuits. *Neuron* **111**, 2675-2692.e9 (2023).

5. Nigro, M. J., Hashikawa-Yamasaki, Y. & Rudy, B. Diversity and Connectivity of Layer 5 Somatostatin-Expressing Interneurons in the Mouse Barrel Cortex. *J. Neurosci.* **38**, 1622–1633 (2018).

6. Xu, H., Jeong, H.-Y., Tremblay, R. & Rudy, B. Neocortical Somatostatin-Expressing GABAergic Interneurons Disinhibit the Thalamorecipient Layer 4. *Neuron* **77**, 155–167 (2013).

7. Muñoz, W., Tremblay, R., Levenstein, D. & Rudy, B. Layer-specific modulation of neocortical dendritic inhibition during active wakefulness. *Science* **355**, 954–959 (2017).

8. Lu, J. *et al.* Selective inhibitory control of pyramidal neuron ensembles and cortical subnetworks by chandelier cells. *Nat Neurosci* **20**, 1377–1383 (2017).

9. Yoshimura, Y. & Callaway, E. M. Fine-scale specificity of cortical networks depends on inhibitory cell type and connectivity. *Nat Neurosci* **8**, 1552–1559 (2005).

10. Krook-Magnuson, E., Varga, C., Lee, S.-H. & Soltesz, I. New dimensions of interneuronal specialization unmasked by principal cell heterogeneity. *Trends in Neurosciences* **35**, 175–184 (2012).

11. Mayer, C. *et al.* Developmental diversification of cortical inhibitory interneurons. *Nature* **555**, 457–462 (2018).

12. Sultan, K. T., Shi, W. & Shi, S.-H. Clonal origins of neocortical interneurons. *Current Opinion in Neurobiology* **26**, 125–131 (2014).

787   13. Harwell, C. C. *et al.* Wide Dispersion and Diversity of Clonally Related Inhibitory Interneurons. *Neuron* **87**,

788   999–1007 (2015).

789   14. Bandler, R. C., Mayer, C. & Fishell, G. Cortical interneuron specification: the juncture of genes, time and

790   geometry. *Current Opinion in Neurobiology* **42**, 17–24 (2017).

791   15. Lim, L., Mi, D., Llorca, A. & Marín, O. Development and Functional Diversification of Cortical Interneurons.

792   *Neuron* **100**, 294–313 (2018).

793   16. Gouwens, N. W. *et al.* Integrated Morphoelectric and Transcriptomic Classification of Cortical GABAergic

794   Cells. *Cell* **183**, 935-953.e19 (2020).

795   17. Allaway, K. C. *et al.* Genetic and epigenetic coordination of cortical interneuron development. *Nature* **597**,

796   693–697 (2021).

797   18. Yao, Z. *et al.* A high-resolution transcriptomic and spatial atlas of cell types in the whole mouse brain. *Nature*

798   **624**, 317–332 (2023).

799   19. Hilscher, M. M., Leão, R. N., Edwards, S. J., Leão, K. E. & Kullander, K. Chrna2-Martinotti Cells

800   Synchronize Layer 5 Type A Pyramidal Cells via Rebound Excitation. *PLOS Biology* **15**, e2001392 (2017).

801   20. Fazzari, P., Mortimer, N., Yabut, O., Vogt, D. & Pla, R. Cortical distribution of GABAergic interneurons is

802   determined by migration time and brain size. *Development* **147**, dev185033 (2020).

803   21. Hevner, R. F., Daza, R. a. M., Englund, C., Kohtz, J. & Fink, A. Postnatal shifts of interneuron position in

804   the neocortex of normal and reeler mice: evidence for inward radial migration. *Neuroscience* **124**, 605–618

805   (2004).

806   22. Lodato, S. *et al.* Excitatory Projection Neuron Subtypes Control the Distribution of Local Inhibitory

807   Interneurons in the Cerebral Cortex. *Neuron* **69**, 763–779 (2011).

808   23. Wester, J. C. *et al.* Neocortical Projection Neurons Instruct Inhibitory Interneuron Circuit Development in a

809   Lineage-Dependent Manner. *Neuron* **102**, 960-975.e6 (2019).

810   24. Ye, Z. *et al.* Instructing Perisomatic Inhibition by Direct Lineage Reprogramming of Neocortical Projection

811   Neurons. *Neuron* **88**, 475–483 (2015).

812   25. Yook, C. *et al.* A TBR1-K228E Mutation Induces Tbr1 Upregulation, Altered Cortical Distribution of

813   Interneurons, Increased Inhibitory Synaptic Transmission, and Autistic-Like Behavioral Deficits in Mice.

814   *Front. Mol. Neurosci.* **12**, (2019).

815   26. Darbandi, S. F. *et al.* Neonatal Tbr1 Dosage Controls Cortical Layer 6 Connectivity. *Neuron* **100**, 831-845.e7

816   (2018).

817   27. Kroon, T. *et al.* Activity-dependent expression of Fezf2 regulates inhibitory synapse formation in pyramidal

818   cells. 2024.01.11.575171 Preprint at https://doi.org/10.1101/2024.01.11.575171 (2024).

819   28. Chen, B. *et al.* The Fezf2-Ctip2 genetic pathway regulates the fate choice of subcortical projection neurons

820   in the developing cerebral cortex. *Proc Natl Acad Sci U S A* **105**, 11382–11387 (2008).

821   29. Molyneaux, B. J., Arlotta, P., Hirata, T., Hibi, M. & Macklis, J. D. Fezl Is Required for the Birth and

822   Specification of Corticospinal Motor Neurons. *Neuron* **47**, 817–831 (2005).

823   30. Stogsdill, J. A. *et al.* Pyramidal neuron subtype diversity governs microglia states in the neocortex. *Nature*

824   **608**, 750–756 (2022).

825   31. Southwell, D. G. *et al.* Intrinsically determined cell death of developing cortical interneurons. *Nature* **491**,

826   109–113 (2012).

827   32. Wong, F. K. *et al.* Pyramidal cell regulation of interneuron survival sculpts cortical networks. *Nature* **557**,

828   668–673 (2018).

829   33. Priya, R. *et al.* Activity Regulates Cell Death within Cortical Interneurons through a Calcineurin-Dependent

830   Mechanism. *Cell Reports* **22**, 1695–1709 (2018).

831   34. Xu, Q., Tam, M. & Anderson, S. A. Fate mapping Nkx2.1-lineage cells in the mouse telencephalon. *Journal*

832   *of Comparative Neurology* **506**, 16–29 (2008).

833   35. La Manno, G. *et al.* RNA velocity of single cells. *Nature* **560**, 494–498 (2018).

834   36. Mòdol, L., Moissidis, M., Selten, M., Oozeer, F. & Marín, O. Somatostatin interneurons control the timing

835   of developmental desynchronization in cortical networks. *Neuron* **112**, 2015-2030.e5 (2024).

836   37. Tuncdemir, S. N. *et al.* Early Somatostatin Interneuron Connectivity Mediates the Maturation of Deep Layer

837   Cortical Circuits. *Neuron* **89**, 521–535 (2016).

838 38. Goldberg, E. M. *et al.* Rapid Developmental Maturation of Neocortical FS Cell Intrinsic Excitability.

839   *Cerebral Cortex* **21**, 666–682 (2011).

840 39. Miyoshi, G., Butt, S. J. B., Takebayashi, H. & Fishell, G. Physiologically Distinct Temporal Cohorts of

841   Cortical Interneurons Arise from Telencephalic Olig2-Expressing Precursors. *J. Neurosci.* **27**, 7786–7798

842   (2007).

843 40. Stickels, R. R. *et al.* Highly sensitive spatial transcriptomics at near-cellular resolution with Slide-seqV2. *Nat*

844   *Biotechnol* **39**, 313–319 (2021).

845 41. Di Bella, D. J. *et al.* Molecular logic of cellular diversification in the mouse cerebral cortex. *Nature* **595**, 554–

846   559 (2021).

847 42. Hirata, T. *et al.* Zinc finger gene fez-like functions in the formation of subplate neurons and thalamocortical

848   axons. *Developmental Dynamics* **230**, 546–556 (2004).

849 43. Wolock, S. L., Lopez, R. & Klein, A. M. Scrublet: Computational Identification of Cell Doublets in Single-

850   Cell Transcriptomic Data. *Cell Systems* **8**, 281-291.e9 (2019).

851 44. Dai, M., Pei, X. & Wang, X.-J. Accurate and fast cell marker gene identification with COSG. *Briefings in*

852   *Bioinformatics* **23**, bbab579 (2022).

853 45. Yao, Z. *et al.* A transcriptomic and epigenomic cell atlas of the mouse primary motor cortex. *Nature* **598**,

854   103–110 (2021).

855 46. Moffitt, J. R. *et al.* High-throughput single-cell gene-expression profiling with multiplexed error-robust

856   fluorescence in situ hybridization. *Proceedings of the National Academy of Sciences* **113**, 11046–11051

857   (2016).

858 47. Zhang, M. *et al.* Spatially resolved cell atlas of the mouse primary motor cortex by MERFISH. *Nature* **598**,

859   137–143 (2021).

860 48. Stringer, C., Wang, T., Michaelos, M. & Pachitariu, M. Cellpose: a generalist algorithm for cellular

861   segmentation. *Nat Methods* **18**, 100–106 (2021).

862 49. Korsunsky, I. *et al.* Fast, sensitive and accurate integration of single-cell data with Harmony. *Nat Methods*

863   **16**, 1289–1296 (2019).

864   50. Rodriques, S. G. *et al.* Slide-seq: A scalable technology for measuring genome-wide expression at high spatial

865   resolution. *Science* **363**, 1463–1467 (2019).

866   51. Stickels, R. *et al.* Library Generation using Slide-seqV2. (2021).

867   52. Cable, D. M. *et al.* Robust decomposition of cell type mixtures in spatial transcriptomics. *Nat Biotechnol* **40**,

868   517–526 (2022).

869   53. Preibisch, S., Saalfeld, S. & Tomancak, P. Globally optimal stitching of tiled 3D microscopic image

870   acquisitions. *Bioinformatics* **25**, 1463–1465 (2009).

871